

Water Resources Research



RESEARCH ARTICLE

10.1029/2020WR027939

Variable Physical Drivers of Near-Surface Turbulence in a Regulated River

Key Points:

- Wind and river flow make comparable contributions to near-surface turbulence in a regulated river
- Dissipation rates predicted from wind speed and flow velocity are in good agreement with observations
- Diel variability in dissipation rates occurs in response to flow regulation and atmospheric forcing

S. Guseva¹ , M. Aurela², A. Cortés³ , R. Kivi⁴ , E. Lotsari^{5,6}, S. MacIntyre³, I. Mammarella⁷ , A. Ojala^{8,9,10}, V. Stepanenko^{11,12,13} , P. Uotila⁷ , A. Vähä⁷ , T. Vesala^{7,9,14} , M. B. Wallin^{15,16} , and A. Lorke¹ 

¹Institute for Environmental Sciences, University of Koblenz-Landau, Landau, Germany, ²Climate Research Programme, Finnish Meteorological Institute, Helsinki, Finland, ³Earth Research Institute, University of California, Santa Barbara, CA, USA, ⁴Space and Earth Observation Centre, Finnish Meteorological Institute, Sodankylä, Finland, ⁵Department of Geographical and Historical Studies, University of Eastern Finland, Joensuu, Finland, ⁶Department of Geography and Geology, University of Turku, Turku, Finland, ⁷Institute of Atmospheric and Earth System Research (INAR)/ Physics, University of Helsinki, Helsinki, Finland, ⁸Ecosystems and Environment Research Programme, Faculty of Biological and Environmental Sciences, University of Helsinki, Helsinki, Finland, ⁹Institute for Atmosphere and Earth System Research/Forest Sciences, Faculty of Agriculture and Forestry, University of Helsinki, Helsinki, Finland, ¹⁰Helsinki Institute of Sustainability Science (HELSUS), Faculty of Biological and Environmental Sciences, University of Helsinki, Helsinki, Finland, ¹¹Laboratory for Supercomputer Modeling of Climate System Processes, Research Computing Center, Lomonosov Moscow State University, Moscow, Russia, ¹²Department of Meteorology and Climatology, Faculty of Geography, Lomonosov Moscow State University, Moscow, Russia, ¹³Moscow Center for Fundamental and Applied Mathematics, Moscow, Russia, ¹⁴Yugra State University, Khanty-Mansiysk, Russia, ¹⁵Department of Earth Sciences: Air, Water and Landscape, Uppsala University, Uppsala, Sweden, ¹⁶Department of Aquatic Sciences and Assessment, Swedish University of Agricultural Sciences, Uppsala, Sweden

Supporting Information:

Supporting Information may be found in the online version of this article.

Correspondence to:

S. Guseva,
guseva@uni-landau.de

Citation:

Guseva, S., Aurela, M., Cortés, A., Kivi, R., Lotsari, E., MacIntyre, S., et al. (2021). Variable physical drivers of near-surface turbulence in a regulated river. *Water Resources Research*, 57, e2020WR027939. <https://doi.org/10.1029/2020WR027939>

Received 13 MAY 2020
Accepted 24 OCT 2021

Abstract Inland waters, such as lakes, reservoirs and rivers, are important sources of climate forcing trace gases. A key parameter that regulates the gas exchange between water and the atmosphere is the gas transfer velocity, which itself is controlled by near-surface turbulence in the water. While in lakes and reservoirs, near-surface turbulence is mainly driven by atmospheric forcing, in shallow rivers and streams it is generated by bottom friction of gravity-forced flow. Large rivers represent a transition between these two cases. Near-surface turbulence has rarely been measured in rivers and the drivers of turbulence have not been quantified. We analyzed continuous measurements of flow velocity and quantified turbulence as the rate of dissipation of turbulent kinetic energy over the ice-free season in a large regulated river in Northern Finland. Measured dissipation rates agreed with predictions from bulk parameters, including mean flow velocity, wind speed, surface heat flux, and with a one-dimensional numerical turbulence model. Values ranged from $\sim 10^{-10} \text{ m}^2 \text{ s}^{-3}$ to $10^{-5} \text{ m}^2 \text{ s}^{-3}$. Atmospheric forcing or gravity was the dominant driver of near-surface turbulence for similar fraction of the time. Large variability in near-surface dissipation rate occurred at diel time scales, when the flow velocity was strongly affected by downstream dam operation. By combining scaling relations for boundary-layer turbulence at the river bed and at the air-water interface, we derived a simple model for estimating the relative contributions of wind speed and bottom friction of river flow as a function of depth.

Plain Language Summary Inland water bodies such as lakes, reservoirs and rivers are an important source of climate forcing trace gases to the atmosphere. Gas exchange between water and the atmosphere is regulated by the gas transfer velocity and the concentration difference between the water surface and the atmosphere. The gas transfer velocity depends on near-surface turbulence, but robust formulations have not been developed for river systems. Their surface area is sufficiently large for meteorological forcing to cause turbulence, as in lakes and reservoirs, but turbulence generated from bed and internal friction of gravity-driven flows is also expected to contribute. Here we quantify near-surface turbulence using data from continuous air and water side measurements conducted over the ice-free season in a large subarctic regulated river in Finland. We find that turbulence, quantified as the dissipation rate of turbulent kinetic energy, is well described using equations for predicting turbulence from meteorological data for sufficiently high wind speeds whereas the contribution from bottom shear dominated at higher flow velocities. A one-dimensional river model successfully captured these processes.

© 2021. The Authors.

This is an open access article under the terms of the [Creative Commons Attribution-NonCommercial-NoDerivs License](https://creativecommons.org/licenses/by-nc-nd/4.0/), which permits use and distribution in any medium, provided the original work is properly cited, the use is non-commercial and no modifications or adaptations are made.

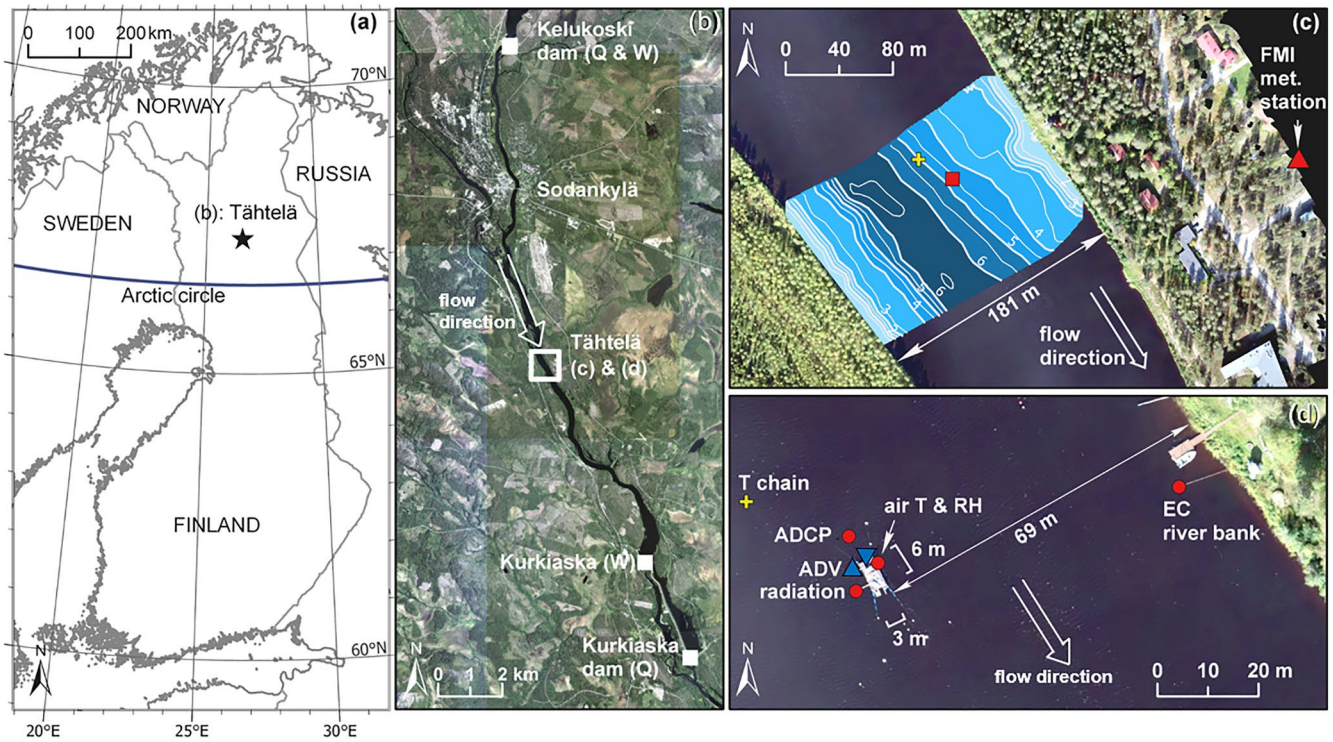
We provide a fundamental model for estimating the relative contributions of atmospheric forcing and bottom friction as a function of depth.

1. Introduction

Inland waters produce, receive, transport and process organic and inorganic carbon and, relative to their surface area, are disproportionately important to regional and global carbon cycling (Aufdenkampe et al., 2011; Cole et al., 2007; Tranvik et al., 2009). River systems are often supersaturated in carbon dioxide (CO₂) and methane (CH₄), and release these radiatively-active gases to the atmosphere (Borges et al., 2015; Richey et al., 2002; Raymond et al., 2013). These gases are derived from terrestrial carbon sources and organic carbon fixed in aquatic ecosystems, and the relative importance of these sources and their response to anthropogenic disturbance remain uncertain in most systems (Alin et al., 2011; Butman & Raymond, 2011).

A key parameter that regulates the gas exchange across the air-water interface is the gas transfer velocity, which is mainly controlled by turbulence on the water side of the interface. Both surface renewal and thin-film theories result in a dependence of the gas transfer velocity on the dissipation rate of turbulent kinetic energy near the water surface (Katul & Liu, 2017; Lamont & Scott, 1970; Zappa et al., 2007). Several mechanisms can contribute to the generation of turbulence in the surface boundary layer (SBL). In lentic aquatic systems, such as lakes and reservoirs, near-surface turbulence is mainly driven by atmospheric forcing, including wind shear, convective cooling and surface wave breaking (Brumer et al., 2017; MacIntyre et al., 2010, 2020). Turbulence generation by wind shear can be described by boundary layer theory and energy dissipation rates scale with wind speed, while decreasing with increasing distance from the water surface (Tedford et al., 2014; Wüest & Lorke, 2003). In the open ocean, there is an increasing contribution of breaking surface waves to near-surface turbulence at wind speeds exceeding 10 m s⁻¹ (Brumer et al., 2017). Convective mixing may occur if the net heat flux across the air-water interface is negative, and under such conditions, dissipation rates of turbulent kinetic energy scale with the surface buoyancy flux although the contribution has been found to be minimal (Bouffard & Wüest, 2019; MacIntyre et al., 2018, 2020). In shallow lotic ecosystems, such as streams, turbulence is mainly generated by bed friction induced by currents, that is, gravity-driven flow, and dissipation rates of turbulent kinetic energy scale with the mean flow velocity and decrease with increasing distance from the bed (Lorke & MacIntyre, 2009). It should be noted, that the term “bottom-generated turbulence” is often used for turbulence generated by bed friction in oceans and lakes. However, in rivers bottom shear can result from wind forcing and from gravity-driven river flow. Here we refer to bottom-generated turbulence as turbulence resulting from the latter forcing. Alin et al. (2011) suggested a conceptual scheme, in which the physical control of the gas transfer velocity in rivers undergoes a transition from the dominance of wind control in large rivers and estuaries toward increasing dominance of water current velocity and depth in smaller channels. Such scheme can provide the basis for a quantitative framework for estimating dissipation rates and gas transfer velocities in rivers, but requires improved mechanistic understanding of the drivers that regulate near-surface turbulence in rivers of different size.

With the need to quantify gas fluxes from rivers, and with minimal measurements of turbulence at this time to test key hypotheses, empirical relations between the gas exchange velocity and bulk flow properties have been developed including channel slope, discharge, mean flow speed, and water depth (Natchimuthu et al., 2017; Raymond et al., 2012; Ulseth et al., 2019; Wallin et al., 2018). Although these parameterizations have mainly been derived for streams, they are applied to larger streams and rivers because direct measurements of gas exchange velocities in large rivers are currently lacking, or restricted to estuaries and tidal rivers. Measurements in an estuary suggested that the principal controlling factor for near-surface dissipation rates was wind and that the surface heat flux and tidal currents played a secondary role (Orton, McGillis, & Zappa, 2010; Orton, Zappa, & McGillis, 2010). These studies underlined the important role of the density stratification in estuaries with seawater intrusions, which reduced the contribution of bed shear to near-surface turbulence. Density stratification can be expected to be less important in inland rivers. However, worldwide many rivers are altered and regulated for human demands (Grill et al., 2019). River regulation is characterized by anthropogenic control of the water level and discharge by dams. Hence, flow regulation is associated with alterations of the magnitude and temporal dynamics of flow velocity (Grill et al., 2019; Poff et al., 2007) and can be expected to affect gas exchange.



The country borders are downloaded from Eurostat (a). The orthomosaic is from National Land Survey of Finland (b).

The aerial orthophoto has been measured on 31st August 2018 by University of Eastern Finland (Pasi Korpelainen) (c and d).

Figure 1. Location of the River Kitinen and the study site (a, b). The study site is marked by the black star in (a) and by the white box in (b). (c) shows the river bathymetry at the study site, text labels refer to water depth in meters. The yellow and red symbols mark in (c), (d) the location of the thermistor chain and floating platform, respectively. The red triangle indicates the location of the land meteorological station operated by the Finnish Meteorological Institute (FMI). (d) Aerial photograph of the instrument platform and locations of instruments. The downward- and upward-facing blue triangles show two locations of the acoustic Doppler velocimeter (ADV) during the first month (June 10 to July 10, 2018) and the remaining period (July 10 to September 24, 2018), respectively. Red circles indicate the locations of the acoustic Doppler current profiler (ADCP), air temperature, relative humidity and radiation sensors and eddy covariance (EC) mast. Large white arrow in (c, b, d) show the flow direction.

In this study we identify the key drivers for near-surface turbulence in a regulated river and their temporal variations from hourly to seasonal time scales. Based on intensive field observations in a subarctic river, we quantify the contributions of gravity-driven flow and atmospheric forcing (wind shear, buoyancy flux, surface waves) to energy dissipation rates near the water surface. We compare our observations to dissipation estimates obtained from bulk parameters using commonly applied scaling relations, as well as to predictions made by a one-dimensional numerical turbulence model. Based on our findings, we derive a mechanistic concept for quantifying the contributions of wind shear and bottom friction to near-surface turbulence, which can be applied to a range of river sizes. To validate our methods for the estimation and predictions of the dissipation rates, we verify the assumption of an equilibrium between production and dissipation of turbulent kinetic energy (TKE) using the model simulations of the individual components of TKE budget.

2. Materials and Methods

2.1. Site Description

The present study was conducted in summer 2018 as part of the KITEK experiment, which was an international measurement campaign designed to improve the understanding of river-atmosphere greenhouse gas exchange. The study combines atmospheric and water-side measurements throughout the ice-free season (June to September) in a regulated river located in continental subarctic climate.

The study was conducted in the River Kitinen, 5 km south of the town Sodankylä in Northern Finland (67.3665°N, 26.6230°E; Figures 1a and 1b). At our study site, the river is a Strahler order 5 river according

Table 1

Hydraulic Parameters During the Observations: S_B [$m\ km^{-1}$] Is Bed Slope, Q [$m^3\ s^{-1}$] Is River Discharge, H [m] Is Water Depth at the Sampling Location, W [m] Is River Width, \bar{u}_{flow} [$m\ s^{-1}$] Is Mean Longitudinal Flow Velocity at 0.4 m Water Depth (See Following Section 2.2), $Re = \frac{\bar{u}_{flow}H}{\nu}$ [-] is Bulk Reynolds Number, ν [$m^2\ s^{-1}$] Kinematic Viscosity of Water (at 15°C), $Fr = \frac{\bar{u}_{flow}}{\sqrt{gH}}$ [-] Is Froude Number, g [$m\ s^{-2}$] Is Gravitational Acceleration

S_B [$m\ km^{-1}$]	Q [$m^3\ s^{-1}$]	H [m]	W [m]	\bar{u}_{flow} [$m\ s^{-1}$]	Re [-]	Fr [-]
0.5	84 (1; 166)	4.2	181	0.13 (0.001; 0.34)	$4.7 \cdot 10^5$; ($2.8 \cdot 10^3$; $1.2 \cdot 10^6$)	0.02 ($1.2 \cdot 10^{-4}$; 0.05)

Note. Each number corresponds to the mean value during the observational period. For temporary varying parameters, the numbers in parentheses are minimum and maximum values.

to HydroSHEDS database (Lehner et al., 2008). The River Kitinen is the main tributary of the River Kemi-joki, which is the longest (ca. 600 km) river in Finland. The construction of two large reservoirs, Lokka and Porttipahta, in the drainage area (ca. 51,000 km²) of the River Kitinen in 1960, as well as seven hydroelectric power plants, modified the river hydrology drastically. One of the consequences is that the spring flooding is no longer present (Åberg et al., 2019). The power company regulates the river discharge at the power stations in such a way that the production of hydroelectricity increases in the morning and decreases during the night. In addition, less electricity is generated on the weekends than on weekdays (Krause, 2011).

The measuring site was located between the two dams of the operating power plants: Kelukoski (ca. 10 km) to the north and Kurkiaska (ca. 10 km) to the south (Figure 1b). The river width at the study location was 181 m and the maximum water depth was 6.5 m. The surrounding area was flat and the mean bed slope was only 0.5 m km⁻¹. The mean Froude number during the observational period was 0.02, which indicates slow subcritical flow (Table 1). A floating platform 6 m long and 3 m wide with measurement instruments was installed near the middle of the river where the water depth reached 4.5 m. The platform had an anchor system with surface buoys. The ropes from the platform corners were attached to surface buoys which were approximately 8–14 m distance from the platform. Ropes from the buoys extended to the bottom where they were fixed to concrete anchors approximately 20–30 m distance from the platform. The ropes connecting the platform, surface buoys and the anchors were tight and made the whole construction stable even in the presence of surface waves.

An eddy covariance (EC) mast was installed at the bank of the river, at a distance of approximately 80 m from the platform. Additionally, meteorological data were collected at meteorological station located at about 247 m east from the floating platform and operated by the Finnish Meteorological Institute (FMI).

2.2. Water-Side Measurements

The instruments and their deployment configurations of the water-side measurements are summarized in Table 2 and Figures 1c and 1d. An Acoustic Doppler Velocimeter (ADV, Nortek Vector) was installed twice during the measurement campaign. For the first month (June 10 to July 10, 2018) it was deployed at the northern (upstream) side of the platform and for the remaining period (July 10 to September 24, 2018) at the western side. The ADV was oriented downwards with its transducer located at a water depth of 0.24–0.25 m in both deployments, providing continuous measurements of flow velocity at the depth of the measurement volume, 0.4 m below the water surface (Figure 2). The instrument measured three components of flow velocity in a nearly cylindrical sampling volume (15 mm diameter, 14.9 mm length), located at a distance of 0.15 m from the transducer. An upward-facing Acoustic Doppler Current Profiler (ADCP, RDI Workhorse 600 kHz) was deployed on the bottom of the river, approximately 10 m upstream of the platform. Its profiling range extended from ~0.7 m above the bottom (including the blanking distance of 0.2 m and the instrument height of 0.4 m) to ~0.3–0.4 m below the surface with a vertical resolution of 0.1 m. The ADCP operated in pulse-coherent mode (high-resolution water profiling mode) and provided along-beam components of flow velocity from four acoustic beams which rise from the transducer at an angle of 20° (transducer diameter: 86 mm, beam width 1.5°). The size of the sampling volume varied from $6.7 \cdot 10^{-4}\ m^3$ near the transducer (at 0.2 m blanking distance) to $2.4 \cdot 10^{-3}\ m^3$ at 0.4 m below the water surface. Three-dimensional velocity vectors at each depth cell were estimated by combining radial along-beam velocities from all four beams. With a beam separation distance of 2.6 m at the water surface (0.4 m depth),

Table 2
Water-Side Measurements Conducted in the River Kitinen

Parameter	Instrument	Period of measurements	Sampling frequency (Hz)	Sampling depth (m)
Flow velocity	ADV Nortek vector	June 10 to September 24, 2018	32	~0.4
Velocity profile	ADCP RDI workhorse 600 kHz	June 7 to September 10, 2018	1–1.5	~0.4–3.5
Water level	RBR duet	June 10 to September 24, 2018	Wave burst mode: every 5 min 512 measurements with 16 Hz	0.43
Water Temperature	RBR solo	June 6 to September 24, 2018	0.1	6 June to 17 June 2018: 0.35, 1.35, 2.35, 3.35, 4.3517 June to 24 September 2018: 0.07, 1.05, 2.05, 3.05, 4.05
Photosynthetically active radiation (PAR)	LI-COR LI-192 Directional PAR sensor (0.3 m, 1 m); LI-COR LI-193 omnidirectional PAR sensor (0.65 m)	May 31 to October 2, 2018	1/60	0.3, 0.65, 0.1

turbulent velocity fluctuations could only be resolved along radial (along-beam) directions, while vertical profiles of mean flow velocities were obtained in Cartesian coordinates. A thermistor chain was deployed to measure water temperature at five different depths (Table 2). Water level fluctuations and surface waves were observed using a wave recorder (RBR duet), which was rigidly deployed on the base of the EC mast at 0.4 m below the water surface. Photosynthetically active radiation (PAR) was measured at the platform at three different water depths. It was used to estimate the attenuation coefficient (k_d [m^{-1}]) in water at noon

using the Beer-Lambert law. Daily mean discharge and water level measurements were provided by the Kurkiaska power station located downstream from the study site (source of data: Finnish Environment Institute SYKE/ Hydrologian ja vesien käytön tietojärjestelmä HYDRO, available at <http://www.syke.fi/avoindata>, last access: 03.01.2019).

2.3. Air-Side Measurements

The meteorological measurements are summarized in Table 3. The eddy covariance system included a USA-1 (METEK) three-axis sonic anemometer/thermometer, which was mounted on a mast in the river at a distance of 10 m from the river bank and at a height of 2 m. The EC system provided mean wind speed \bar{u}_{wind} [m s^{-1}], wind direction w_{dir} [$^\circ$] and atmospheric friction velocity u_{*EC} [m s^{-1}] at 2 m height. Gaps in the time series measurements of wind speed and direction measured at the platform were filled using linearly regressed values from the corresponding station on land (FMI). We used incoming shortwave and longwave radiation from the land station, which were nearly identical to the values measured at the platform, but without gaps. The outgoing shortwave radiation was calculated as a product of albedo and incoming shortwave radiation, where albedo was estimated from Fresnel's Law (Neumann & Pierson, 1966). Outgoing longwave radiation was calculated as a function of surface water temperature (MacIntyre et al., 2002). Air temperature and relative humidity were measured at the platform (Rotronic HC2-S3CO3), and were also gap-filled using linear regression between the platform data and the land station data.

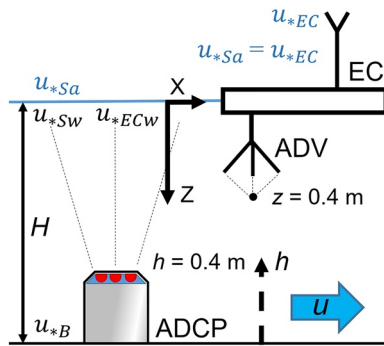


Figure 2. Schematic representation of (a) instruments location (Acoustic Doppler Velocimeter [ADV] and Acoustic Doppler Current Profiler [ADCP]). The upward-facing ADCP was installed on the river bottom. The sampling volume of the downward-oriented ADV was at 0.4 m below the water surface (black dot). Vertical coordinate z [m] is measured positive downward, h [m] corresponds to the distance from the bottom. Blue labels u_{*Sa} , u_{*EC} [m s^{-1}] correspond to the surface air-side friction and atmospheric friction velocity. The former is the generic descriptor of the air-side friction velocity and the latter is calculated from eddy covariance (EC) measurements 2 m above the water surface. In the atmospheric boundary layer, we assume a constant shear stress distribution, thus, both friction velocities are equal. Black labels u_{*Sw} and u_{*ECw} indicate generic surface water-side friction velocity and surface water-side friction velocity converted from u_{*EC} using the assumption of continuity of shearing stress across the air-water interface, respectively. u_{*B} is bed friction velocity. The large blue arrow indicates the direction of the mean flow velocity (u).

Table 3
Meteorological Measurements Conducted at the Study Site

Parameter	Instrument/Manufacturer	Period of measurements	Sampling frequency (Hz)	Instrument height (m)	Location
Wind speed, wind direction, atmospheric friction velocity	USA-1 (METEK)	May 29 to 17 October, 2018	10	2	>10 m from river bank
Wind speed, wind direction	UA2D Adolf Thies GmbH & Co. KG	May 01 to October 31, 2018	1/60	22.7	Land meteorological station (FMI)
Incoming short-and longwave radiation	CM11, Kipp & Zonen B.V.	May 01 to October 31, 2018	1/60	17.5	Land meteorological station (FMI)
Air temperature, relative humidity	Rotronic HC2-S3CO3	31 May to 20 September 2018	1/60	2	Measurement platform
Air temperature	Pt100 sensor, Pentronic AB	May 01 to October 31, 2018	1/60	2	Land meteorological station (FMI)
Relative humidity	HMP155D, Vaisala Oy	May 01 to October 17, 2018	1/60	2	Land meteorological station (FMI)

2.4. Data Processing

2.4.1. Turbulent Kinetic Energy Budget

In the turbulent boundary layer, we consider the following budget of turbulent kinetic energy K [$\text{m}^2 \text{s}^{-2}$] (Foken & Napo, 2008; Kundu et al., 2010):

$$\underbrace{\frac{\partial K}{\partial t}}_{(1)} + \underbrace{\bar{u}_j \frac{\partial \bar{K}}{\partial x_j}}_{(2)} + \underbrace{\frac{\partial \bar{u}'_j K}{\partial x_j}}_{(3)} = - \underbrace{\frac{1}{\rho_w} \frac{\partial \bar{u}'_i p'}{\partial x_i}}_{(4)} - \underbrace{g \alpha \bar{w}' T'}_{(5)} - \underbrace{\bar{u}'_i \bar{u}'_j \frac{\partial \bar{u}_i}{\partial x_j}}_{(6)} - \underbrace{\varepsilon}_{(7)} \quad (1)$$

where $K = \frac{1}{2} \bar{u}'_i{}^2$ is the turbulent kinetic energy, \bar{u}_i , $i = 1, 2, 3$ which corresponds to u, v, w , u'_i which corresponds to u', v', w' [m s^{-1}] are the mean velocities and the turbulent velocity fluctuations, respectively, resulted from Reynolds decomposition of each of the velocity component. ρ_w [kg m^{-3}] is the water density, p' [Pa] are the turbulent pressure fluctuations, x_i [m] are the coordinates where x_1, x_2, x_3 correspond to x, y, z , T' [K] are the temperature fluctuations, ε [W m^{-2}] is the dissipation rate of turbulent kinetic energy (summation convention is implied over the indices i and j). For steady-state conditions and homogeneous turbulence, the rate-of-change of TKE term (1) and the turbulent transport terms (2) – (3), as well as pressure correlation term (4) are neglected. By further assuming two-dimensional flow conditions (uniform flow except for vertical variations of the mean longitudinal flow velocity \bar{u}_{flow} [m s^{-1}]), leads to an approximate equilibrium between the sum of the shear production term (6) and buoyant production or consumption term (5) and the rate of energy dissipation (7) (Equation 2).

$$\varepsilon = -g \alpha \bar{w}' T' - \bar{w}' u' \frac{\partial \bar{u}_{\text{flow}}}{\partial z} \quad (2)$$

Note that, in comparison with, for example (Nikora & Roy, 2012), we consider the buoyancy term here, as a source of TKE during convective cooling.

2.4.2. Estimation of Near-Surface Dissipation Rates From ADV Data

Data analysis procedures for the ADV and the ADCP were similar in that, first, the data went through quality control procedures and then dissipation rates were computed using the inertial subrange method. The ADV resolved the vertical velocity component of flow directly. It had high quality data and could be used to estimate dissipation rates when surface waves were present. Thus, dissipation rates from the ADV measurements were primarily used in the results and discussion sections when characterizing near-surface turbulence. The sampling rate of the ADV was 32 Hz. Data were quality-checked by removing measurements with a correlation magnitude less than 70% (a standard statistical measure of velocity data quality [Nortek, 2015]). Outliers were removed following the procedures described in (Goring & Nikora, 2002;

Wahl, 2003). Subsequent analysis was performed for 10 min periods following established methods (Cannon & Troy, 2018; Guerra & Thomson, 2017; Jabbari et al., 2020; McCaffrey et al., 2015; McMillan & Hay, 2017; Orton, McGillis, & Zappa, 2010). If more than 20% of the data within each period were removed by the quality check, then the period was discarded, otherwise the missing velocities were linearly interpolated. In Text S1 in Supporting Information S1 we demonstrate that the chosen threshold of 20% results in an uncertainty of dissipation rate estimates of less than 10% (Figure S1 in Supporting Information S1). Velocities measured in instrument coordinates were rotated into the direction of the mean flow for each interval. Mean flow velocity was calculated for each 10 min time interval as the mean longitudinal velocity component \bar{u}_{flow} . In total, 11% of the data were removed during quality screening and averaging.

Dissipation rates of turbulent kinetic energy ε_{ADV} [W kg^{-1}] were estimated using the inertial dissipation technique also known as inertial subrange fitting (ISF), following (Bluteau et al., 2011). This method is based on general theories of turbulence describing a cascade of energy from the larger to the smaller scales (Tennekes & Lumley, 1972) and an implicit assumption of an equilibrium between production and dissipation of TKE. We estimated the dissipation rate using the following equation:

$$\varepsilon = \left(\frac{E(k)}{A\alpha_K k^{-5/3}} \right)^{3/2}. \quad (3)$$

Here, E [$\text{m}^3 \text{s}^{-2} \text{rad}^{-1}$] is the one-dimensional wave number spectrum of turbulent velocity fluctuations. $\alpha_K = 1.5$ [-] is the Kolmogorov constant, k is the longitudinal wave number [rad m^{-1}], and A is a constant which depends on the direction of velocity fluctuations: for vertical and transversal components $A = \frac{4}{3} \times \frac{18}{55}$ [-] and for horizontal component $A = 1 \times \frac{18}{55}$ [-] (Pope, 2000).

Velocity power spectra in the frequency domain $S(\omega)$ [$\text{m}^2 \text{s}^{-1} \text{rad}^{-1}$] were calculated using Welch's method (Thomson & Emery, 2001). Each 10 min segment of velocity time series was divided into overlapping (50%) sections with 8192 individual samples on which a fast Fourier transform was applied after subtraction of a linear trend and multiplication with a Hanning window function. Power spectra were estimated as the average squared magnitude of the periodograms. We converted the spectra from frequency to the wave number domain ($\omega = \bar{u}_{\text{flow}} k$) using Taylor's frozen turbulence hypothesis, which assumes that the turbulent flow does not change its characteristics while passing through the sensor and that turbulent velocity fluctuations are much smaller than the mean flow. The validity of this approach was tested as $(\overline{u_i^2})^{1/2} / \bar{u}_{\text{flow}} \leq 0.15$ (Bluteau et al., 2011).

The spectral range used for inertial subrange fitting was limited by the instrument noise at a high frequency limit ω_{up} [rad s^{-1}] and by the size of energy-containing eddies at a lower frequency limit ω_{low} [rad s^{-1}]. We defined the upper cutoff frequency as the frequency for which the ratio of power spectral density to the noise level became smaller than one. The noise level was calculated for each spectrum as the logarithmic mean of S at frequencies larger than 50 rad s^{-1} where noise was always observed even for high flow velocity, see Figure 3a. The lower frequency limit was estimated by identifying a breakpoint in spectral slope at the beginning of the inertial subrange (IS) in each spectrum (see Text S2, Figure S2a in Supporting Information S1). If this breakpoint corresponded to the distance larger than the distance to the boundary $-l = 0.4 \text{ m}$ and 4.2 m for vertical and horizontal velocity components, respectively, then the lower IS limit was set to the frequencies corresponding to this distance ($\omega_{\text{low}} = 2\pi\bar{u}_{\text{flow}}/l$) (see an example for vertical component in Figure S2b in Supporting Information S1).

Many spectra had a pronounced peak caused by surface waves ($\sim 10 \text{ rad s}^{-1}$ or 1 s period, see Figure 3b). For these spectra, an upper frequency limit for ISF was defined as the frequency where the function $f = S(\omega) \cdot \omega$ had a minimum value within the interval $0.5 \leq \omega_{\text{up}} \leq 3$ [rad s^{-1}]. The minimum marks the transition from the $-5/3$ power law to the wave peak.

Following the suggestions in Bluteau et al. (2011), we applied the following quality criteria to the inertial subrange fits: (a) validity of Taylor's frozen turbulence hypothesis (15% of the fits were rejected); (b) coefficient of determination should be larger than 0 (26% of fits were rejected). In addition, the following optional quality criterion was applied: (c) length of the fitted inertial subrange (10% of fits were rejected). We applied the three criteria to all the data (the threshold for the last one was 10/8 of a decade as an compromise

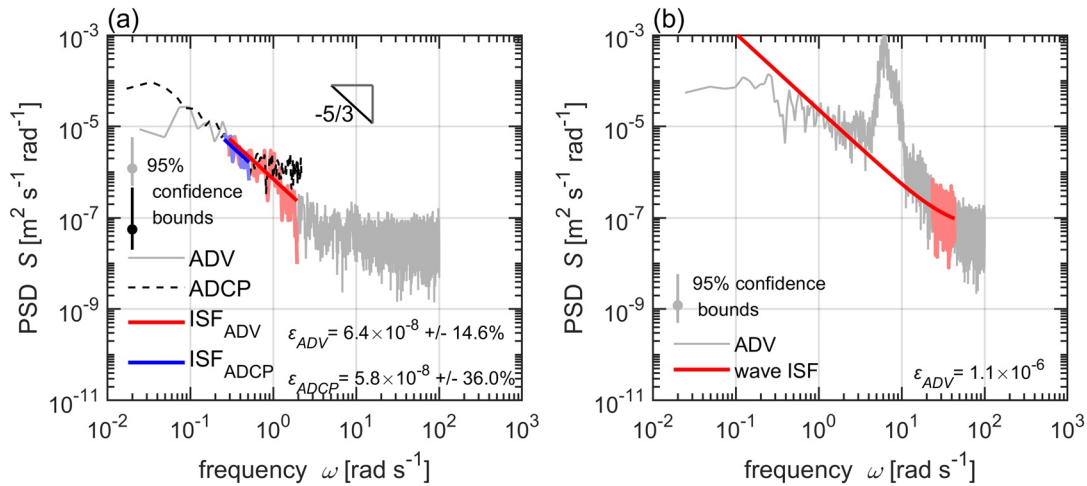


Figure 3. (a) Typical frequency spectrum (power spectral density, PSD) of vertical velocity fluctuations measured by ADV (gray line) and along-beam velocity fluctuations measured by ADCP (dashed black line) for a period without surface waves. Blue and red parts of the spectra represent the selected range for estimating dissipation rates by inertial subrange fitting (ISF, $-5/3$ slope) for ADCP and ADV, respectively. Thick blue and red lines show the corresponding fits. The dissipation rates obtained from ISF ϵ_{ADV} , ϵ_{ADCP} [W kg^{-1}] with confidence bounds (in percent) are provided as labels. Gray and black lines with dots indicate the 95% confidence bounds of the spectra for ADV and ADCP, respectively. (b) ADV frequency spectrum for a period with surface waves (wave peak at around 10 rad s^{-1}). The frequency range marked by red color was used for spectral fitting of the wave affected inertial subrange method (Equation 4). The extrapolated fit from the wave-affected part is shown as a thick red line.

between reasonable amount of data and avoiding too short inertial subrange) and rejected fits were discarded from further analyses of dissipation rates. Application of these three criteria led to 58% reduction of the fits.

We visually inspected the spectra of all three velocity components. Most of the horizontal and transversal velocity spectra were strongly contaminated by noise (see a typical example in Figure S3a in Supporting Information S1). In contrast to that, the vertical component was found to be less affected by noise. To validate the assumption of isotropic turbulence, we compared the quality assured dissipation rate estimates from horizontal and vertical velocity components (see Figure S3b in Supporting Information S1). We found a good agreement on average, however, at higher dissipation rates there was a discrepancy of at least a factor of 3–5. We used only the vertical velocity component for the calculation of dissipation rates, as in other studies, (e.g. Feddersen et al., 2007).

When surface waves were present, we fitted spectra at frequencies higher than the surface waves and lower than the noise limit (see Figure 3b). Advection by wave orbital velocities additionally was accounted for:

$$\epsilon = \exp \left\langle \ln \left(\frac{(S_{ww}(\omega) - \text{Noise level}) \omega^{5/3}}{\alpha_K J_{ww}} \right)^{3/2} \right\rangle, \quad (4)$$

where $J_{ww} = f(\sigma_1, \sigma_2, \sigma_3, \bar{u}, \bar{v})$ is a function describing the effect of the wave advection in terms of the standard deviations of all three velocity components σ , and mean horizontal flow velocities (\bar{u}, \bar{v}) (Gerbi et al., 2009). The subscript “ww” is used for vertical velocity component. The angled brackets denote averaging over all frequencies ω for which the inertial subrange fit was applied. This method is a slightly modified version of the one proposed by (Feddersen et al., 2007). The spectra which were affected by surface waves and the range of the frequencies for wave peaks were selected manually. These selected spectra were fitted according to Equation 4. A comparison of both fitting procedures for spectra where an inertial subrange could be fitted at both sides of the wave peak, revealed good agreement of the resulting dissipation rates. Resulting dissipation rates consisted of 54% and 46% estimates using Equations 3 and 4, respectively.

To exclude time periods for which the observed flow was potentially affected by the platform, we discarded dissipation rate estimates for which the sampling location was at the downwind end of the platform, that is, for wind direction (a) $80^\circ \leq w_{dir} \leq 245^\circ$ for the first and (b) $20^\circ \leq w_{dir} \leq 150^\circ$ for the second deployment.

This led to a further 25% reduction of the quality-checked data resulting in a total of 7,452 dissipation rate estimates based on ADV data (0.4 m water depth).

2.4.3. Estimation of Dissipation Rates From ADCP Data

The overall procedure to analyze ADCP data was similar to that with the ADV. That is, the first steps involved obtaining valid data using quality controls followed by calculating dissipation rates in the inertial subrange. Measurements with a magnitude of signal correlation less than 70 were removed and velocity time series at each depth were despiked using the same parameters as for the ADV data. For the first 33 days, we applied a bin mapping procedure using linear interpolation (Ott, 2002) due to a significant instrument tilt during this deployment ($\sim 8^\circ$). Frequently occurring losses of connection to the ADCP resulted in missing data and a slight reduction of actual sampling frequency. If the number of missing velocity measurements in 10 min analysis intervals was less than 20%, we applied linear interpolation to fill these gaps using the mean sampling frequency for this period.

Velocities were measured in beam coordinates, which were transformed to orthogonal (instrument) coordinates before being rotated into the mean flow direction (longitudinal, transversal and vertical velocity components) for 10 min averaging intervals. After quality screening and averaging, the temporal coverage of valid velocity measurements was $\sim 50\%$ of the total deployment duration in the middle of the water column, and slightly less (44%) near the water surface (0.4 m water depth).

Frequency spectra were calculated from beam velocities over 10 min periods (number of samples used for the fast Fourier transform is 256) and log-averaged over all 4 beams. The identification of the lower and upper frequencies of the inertial subrange was the same as described above for the ADV. For each individual depth the distance to the boundary (except cases when the breakpoint in the in the optimization procedure was smaller than this distance), was fixed as the lower frequency limit.

Since the ADCP measures velocity fluctuations along the four acoustic beams, the direction of the turbulent velocity fluctuations, that is, the constant A (Equation 3) is undetermined. In this study the constant was set to $A = 1.16 \times \frac{18}{55}$, which corresponds to the average of 1 and 4/3. We applied the same quality criteria to spectral fits as for the ADV data.

The sampling frequency of the ADCP was too low to resolve wave orbital velocities, and we could not estimate dissipation rates during wave-affected periods. As described above, we primarily used the ADV data in subsequent analyses. The ADCP based estimates are used in Sections 2.6, 3.2, where we specifically analyze bottom-generated turbulence and provide vertical profiles of dissipation rates.

2.4.4. Shear Stress Obtained From Eddy Covariance

A double rotation of the coordinate system was performed with the wind velocity measurements of the anemometer (McMillen, 1988). The atmospheric friction velocity was calculated from the original 10 Hz data as 5 min block-averages as a square root of the Reynolds stress in the air:

$$u_{*EC} = \left(\overline{u'_{EC} w'_{EC}}^2 + \overline{v'_{EC} w'_{EC}}^2 \right)^{\frac{1}{4}}. \quad (5)$$

Here, the subscript “EC” is used showing that these turbulent velocity fluctuations were measured in the air. Screening for weak turbulence with a specific friction velocity limit was not performed, but the cases with upward momentum flux ($\overline{u'_{EC} w'_{EC}} < 0$) were discarded. The 5 min u_{*EC} , wind speed and wind direction data were further averaged to 10-min mean values to enable direct comparison with other data. Acceptable wind directions were $151^\circ \leq w_{dir} \leq 190^\circ$ and $290^\circ \leq w_{dir} \leq 323^\circ$ to ensure sufficient fetch with an open water surface.

2.5. Turbulence From Atmospheric Forcing

To estimate dissipation rates in the water from bulk measurements of atmospheric forcing, we used Monin-Obukhov similarity scaling described in Tedford et al. (2014). During periods of heating of the water surface (the surface buoyancy flux, $J_{BO} > 0$ [W kg^{-1}]), dissipation rates were estimated as:

$$\varepsilon_{\text{SBL}} = \varepsilon_{\text{SBL, wind}} = C_1 \frac{u_{*Sw}^3}{\kappa z}, \quad (6)$$

where $\kappa = 0.41$ [-] is the von Kármán constant, $C_1 = 0.6$ is a constant, z [m] is the distance from the water surface. u_{*Sw} [m s⁻¹] is the surface water-side friction velocity computed from surface wind shear stress τ_s [N m⁻²] assuming continuity of shear stress at the interface $\tau_s = \rho_a u_{*Sa}^2 = \rho_w u_{*Sw}^2$, where ρ_a [kg m⁻³] is the air density, u_{*Sa} [m s⁻¹] is the surface air-side friction velocity. Using this assumption we calculated $u_{*Sw} = (\tau_s / \rho_w)^{1/2}$. Surface wind shear stress was calculated from the wind speed as $\tau_s = \rho_a C_{Da} \bar{u}_{wind}^2$, where C_{Da} [-] is the drag coefficient. We assumed a neutral drag coefficient at 10 m height of $C_{Da 10m} = 1.3 \cdot 10^{-3}$ (Foken & Napo, 2008), which gives $C_{Da 2m} = 1.8 \cdot 10^{-3}$ at the 2 m measurement height using boundary-layer scaling. Note, that “neutral” refers to the neutral stratification in the atmosphere. $C_{Da 2m}$ was corrected for atmospheric stability following (Hicks, 1972).

The buoyancy flux was calculated as $J_{BO} = g\alpha Q_{heat} / (C_{pw}\rho_w)$ [W kg⁻¹], where Q_{heat} [W m⁻²] is the effective heat flux at the water surface, α is the thermal expansion coefficient of water, C_{pw} [J kg⁻¹ °C⁻¹] is the specific heat capacity of water. The surface heat flux was computed as the sum of latent heat flux, sensible heat flux and net longwave radiation, and the effective heat flux for the actively mixing layer as the sum of the surface heat flux plus the shortwave radiation retained within the actively mixing layer. The mixing layer depth was estimated as the depth where the water temperature difference from the surface was exceeding 0.02°C. All calculations above were based on formulations from (Imberger, 1985; MacIntyre et al., 2002, 2014).

During water cooling ($J_{BO} \leq 0$), when convective mixing also contributed to the dissipation rate (Tedford et al., 2014), ε_{SBL} was estimated as:

$$\varepsilon_{\text{SBL}} = \varepsilon_{\text{SBL, wind}} + \varepsilon_{\text{SBL, buoy}} = C_1 \frac{u_{*Sw}^3}{\kappa z} + 0.77 |J_{BO}|, \quad (7)$$

Additionally, we used surface boundary layer scaling to estimate wind-generated energy dissipation rates (Equation 6) in the water from atmospheric momentum fluxes measured by EC:

$$\varepsilon_{\text{SBL,EC}} = C_1 \frac{u_{*ECw}^3}{\kappa z}, \quad (8)$$

where the surface water-side friction velocity u_{*ECw} was estimated from the atmospheric friction velocity u_{*EC} calculated from the EC system as $u_{*ECw} = u_{*EC}(\rho_a / \rho_w)^{1/2}$. Shear stress is assumed constant in the atmospheric boundary layer ($u_{*EC} = u_{*Sa}$).

2.6. Bottom-Generated Turbulence

In addition to turbulence generated by atmospheric forcing, we consider the contribution of bed friction of gravity-driven river flow. This source of turbulence comes from the mean kinetic energy through the shear production term (6) in Equation 1. We used the variance of ADCP beam velocities to compute vertical profiles of Reynolds shear stresses $\tau_T = \left(\overline{-u'w'^2} + \overline{-v'w'^2} \right)^{1/2}$ [N m⁻²] following (Stacey et al., 1999). The bed friction velocity u_{*B} [m s⁻¹] was calculated as:

$$u_{*B} = \left(\frac{\tau_T}{\rho_w \left(1 - \frac{h}{H}\right)} \right)^{1/2}, \quad (9)$$

where h [m] is the distance from the bottom, H is the total water depth at the ADCP location.

To estimate the near-surface dissipation rates generated by turbulence production by bed shear we used three approaches, which are all based on the assumption of a steady, two-dimensional boundary-layer flow. The first simple dissipation scaling is based on the assumption that the shear stress is constant over the water column and equal to bed shear stress τ_b [N m⁻²]:

$$\varepsilon_{\text{BBL}} = \frac{u_{*B}^3}{\kappa h}. \quad (10)$$

A commonly used empirical approach in open channel flows, where the shear stress is decreasing linearly from the bed to zero at the water surface (Nezu, 1977), results in a stronger exponential decay of dissipation rates with distance from the bed:

$$\epsilon_{\text{BBL, Nezu}} = \frac{u_{*B}^3}{H} \frac{E}{\sqrt{h/H}} \exp\left(-\frac{3h}{H}\right), \quad (11)$$

where E [-] is an empirical constant for which we assigned a value of $E = 9.8$, as suggested by Nezu (1977). In addition, we used the model proposed in Nikora and Smart (1996):

$$\epsilon_{\text{BBL, NS}} = \frac{u_{*B}^3}{\kappa h} \left(1 - \frac{h}{H}\right), \quad (12)$$

where apart from linearly-decreasing shear stress a logarithmic profile of the mean flow velocity is taken into account. Note, that the assumption of an equilibrium between production and dissipation of turbulent kinetic energy is implied in all above equations and density stratification is not considered.

To identify periods when bed shear stress was the dominating generation mechanism for near surface turbulence, we estimated u_{*B} from ADCP data (Equation 9) as the mean value over 18 bins (0.7–2.4 m above the bed). We then selected cases when the dissipation rate at 0.4 m water depth predicted by Equation 10 exceeded the dissipation rate from atmospheric forcing (Equation 6 and 7). For these cases, we compared the vertical distribution of dissipation rates obtained from ADCP data with the three scaling approaches described by Equation 10–12.

For the selected cases for which bed-shear was the dominating source of near-surface turbulence, we estimated the bed drag coefficient C_{Dw} [-], which relates bed shear stress to the mean flow velocity at a given height above the bed:

$$C_{Dw} = \frac{u_{*B}^2}{\bar{u}_{\text{flow } 1m}^2}. \quad (13)$$

C_{Dw} was first estimated for a height of 1 m above the bed using the mean flow velocity measured by the ADCP. Unrealistically high values of the drag coefficient were excluded from averaging. We chose an upper threshold of ($C_{Dw} \leq 7.4 \cdot 10^{-3}$, which corresponds to the upper limit of Manning's roughness coefficient $n_M = 0.035 \text{ s m}^{-1/3}$ reported for the rivers with sand bed and the straight uniform channel where grain roughness is predominant (Arcement & Schneider, 1989; Chow, 1959). To take advantage of the longer time series of mean flow velocity measured by the ADV, we subsequently scaled the bed drag coefficient to 0.4 m water depth following two equations where we first derived the bed roughness length z_0 [m]:

$$z_0 = h \cdot e^{-\frac{\kappa}{\sqrt{C_{Dw}}}}, \quad (14)$$

where $h = 1$ m. Then we calculated the bed drag coefficient at 0.4 m water depth ($h = 3.8$ m):

$$C_{Dw} = \frac{\kappa^2}{\ln\left(\frac{h}{z_0}\right)^2}. \quad (15)$$

By combining expressions for the bed shear stress $\tau_B = \rho_w C_{Dw} \bar{u}_{\text{flow}}^2$, and the bed friction velocity $u_{*B} = (\tau_B / \rho_w)^{1/2}$ and Equation 10, the mean flow velocity measured by the ADV was used to estimate the near-surface dissipation rate generated by bed shear ($\epsilon_{\text{BBL, ADV}}$) as:

$$\epsilon_{\text{BBL, ADV}} = C_{Dw}^{\frac{3}{2}} \frac{\bar{u}_{\text{flow}}^3}{\kappa h}. \quad (16)$$

2.7. One-Dimensional $k - \epsilon$ Model

Both bottom shear stress and atmospheric forcing are taken into account while simulating dissipation rates below the water surface using a vertically resolving turbulence model of a river flow. The one-dimensional (in vertical direction) modeling of turbulent river flow should be sufficient to reproduce the vertical structure of thermo- and hydrodynamic properties, if the marginal effects at river banks are negligible; this is the case when depth-to-width ratio is small (about 0.02 for the River Kitinen at the location of the raft). The $k - \epsilon$ model used in this study is a 1D version of Reynolds-Averaged Navier-Stokes (RANS) equation system. This system is an exact result of spatial averaging of 3D RANS-equations over a horizontal cross-section of a river stream, in which the shape of horizontal and vertical cross-sections are assumed rectangular, neglecting heat and momentum fluxes at the channel banks and omitting longitudinal advection; the system is provided with boundary conditions from atmospheric and river discharge measurements (the complete description of the model is given in Text S4 in Supporting Information S1). The full system is solved using LAKE2.0 model code (Stepanenko et al., 2016) as it uses horizontal averaging of thermo- and hydrodynamic equations as well. The only modification to the lake model algorithm was an addition of a method to compute longitudinal pressure gradient, driving the river flow (Text S4 in Supporting Information S1).

The model provided TKE transport terms, which we use in Section 3.6 to verify the assumption of an equilibrium between the production and the dissipation underlying dissipation rate estimates.

2.8. Statistical Analyses

Cumulative distribution functions of dissipation rate estimates are approximately lognormal (Baker & Gibson, 1987). Averaging of dissipation rates was therefore done with log-transformed values. Similarly, also estimates of the bottom drag coefficient log-averaged. For visual comparison of different dissipation rate estimates we applied a bin-averaging procedure, which is described in Supporting Information S1 (Text S3, Figure S8).

3. Results

3.1. Overview of the Measurements

The variations of wind speed, flow velocity and surface buoyancy flux as the main drivers for near-surface turbulence are shown in Figure 4. Wind speed varied over diel and synoptic scales with a range of 0 and 8.4 m s^{-1} . Mean flow velocity also changed over diel cycles due to the downstream dam operations and ranged between 0.001 and 0.34 m s^{-1} . River discharge at the downstream Kurkiaska power station (Figure 4b) varied between 1 and $166 \text{ m}^3 \text{ s}^{-1}$, with no pronounced seasonal pattern. The mean discharge during the time period from June 1 to September 30 was $84 \text{ m}^3 \text{ s}^{-1}$. Daily mean measured flow velocity and the discharge were strongly correlated ($\rho = 0.9$, $p < 0.05$, where ρ is a correlation coefficient and p is a significance level for the correlation coefficient). The surface buoyancy flux generally showed a pronounced diel pattern with seasonally varying amplitude. Maximum ($3.2 \cdot 10^{-7} \text{ W kg}^{-1}$) and minimum ($-1.7 \cdot 10^{-7} \text{ W kg}^{-1}$) values were observed at the beginning of August. Nighttime buoyancy fluxes were negative throughout the observational period as expected and indicative of periods when convective mixing could occur. The dissipation rate at 0.4 m depth varied between $9.7 \cdot 10^{-10}$ and $2.4 \cdot 10^{-5} \text{ W kg}^{-1}$ (Figure 4d). Dissipation rates less than $10^{-8} \text{ W kg}^{-1}$ were observed when flow velocities were low, that is, at low discharge.

Air temperature varied between -0.8°C on September 15 and 30.3°C on July 13 and also showed a diel pattern (Figure S4a in Supporting Information S1). Surface water temperature increased during summer, reaching its maximum value of 23°C on August 2, and slowly decreased toward autumn to the minimum value of 8.7°C on September 22. Weak thermal stratification developed primarily during the first half of the summer June–July (Figure S5 in Supporting Information S1). The maximum value of the temperature difference between the surface and bottom was 2.3°C on June 18 (Figure S5a in Supporting Information S1). Using a threshold for the temperature difference between surface and bottom of 0.05°C (Bormans & Webster, 1997), stratification was observed on 41 days and persisted for 38% of the observational period.

Significant wave height H_{sig} (defined as the average wave height, from trough to crest, of the highest one-third of the waves) was correlated to wind speed ($\rho = 0.7$, $p < 0.05$) and was mostly below 0.05 m reaching

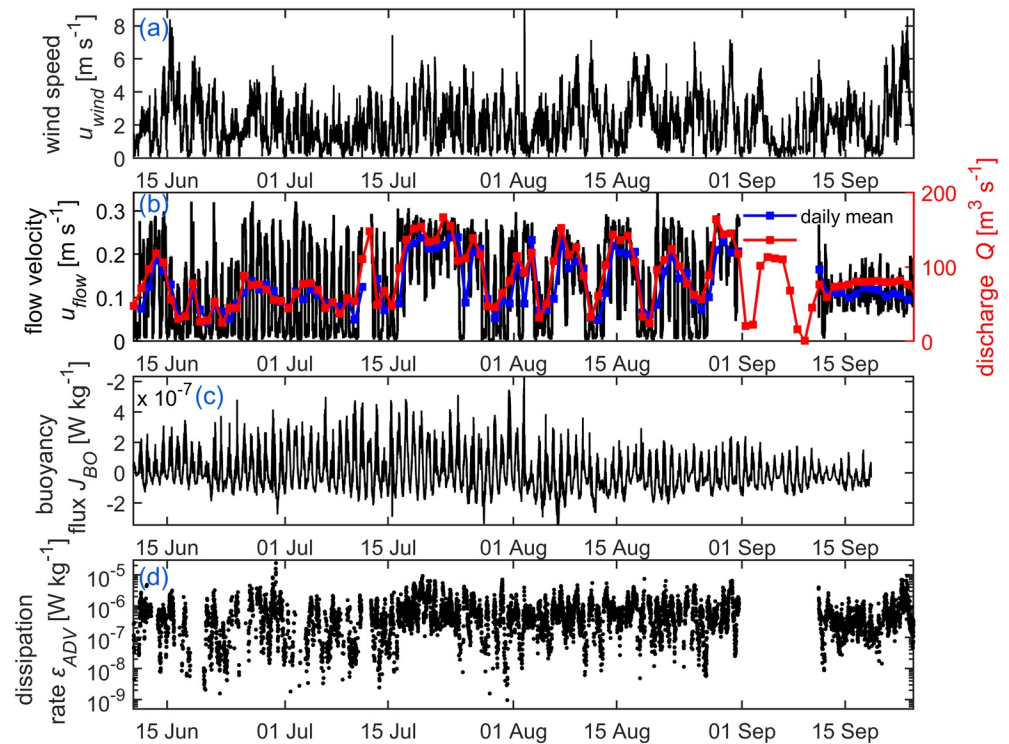


Figure 4. Time series of drivers of near-surface turbulence during the study period: (a) wind speed; (b) longitudinal flow velocity at 0.4 m water depth (ADV, black line), daily mean flow velocity (blue line) and daily mean discharge at Kurkiaska power station (red line with square symbols); (c) buoyancy flux; (d) dissipation rate of turbulent kinetic energy at 0.4 m depth. Except for daily mean values in (b), all data are shown with 10 min resolution.

a maximum value of 0.11 m (Figure S4c in Supporting Information S1). We found weaker correlation between H_{sig} and \bar{u}_{wind} when the wind blew along the main flow direction ($\rho = 0.5$, $p < 0.05$, Figure S6a in Supporting Information S1) in comparison with a relatively strong correlation and linear relationship ($\rho = 0.8$, $p < 0.05$) when the wind direction was in opposition to the main flow direction (Figure S6b in Supporting Information S1).

The diel variability in flow was not only observed at the surface but throughout the full water column (Figure 5). Maxima occurred during daytime (Figures 5b and 5c). The change from high to low flow velocity occurred rapidly, with mean flow velocity often decreasing by 50% within 30–60 min. The direction of the mean flow near the water surface was aligned either with the wind direction or with the direction of river flow (Figure 5a). During the day, when flow velocities and wind were elevated, incoming heat was sometimes mixed throughout the water column and water temperature increased; on the other days temperature declined. After flow speed and wind speed decreased at night, weak thermal stratification occurred and persisted until midnight (see 1–2 July in Figure 5d). Stratification usually persisted for several hours, before it was disrupted by a rapid increase in flow or by convective mixing.

3.2. Bottom-Generated Turbulence

When bed-shear was expected to dominate near-surface dissipation rates ($n = 2,967$), the temporarily averaged dissipation rate estimated from ADCP measurements were highest near the bottom (maximum value of $3.7 \cdot 10^{-6} \text{ W kg}^{-1}$ at a distance of 0.7 m above the bottom) and decreased by a factor of five to $7.1 \cdot 10^{-7} \text{ W kg}^{-1}$ near the water surface (Figure 6a). The vertical profile agreed well with the simple dissipation scaling based on assumption of the constant shear stress distribution (Equation 10). The extrapolation to 0.4 m water depth was in close agreement with the mean dissipation rate estimated from ADV measurements for the selected cases. This agreement was unexpected as the extrapolation of the dissipation rates up to water surface using Equations 10 and 12 is only valid for a distance from the bottom over which the velocity profile

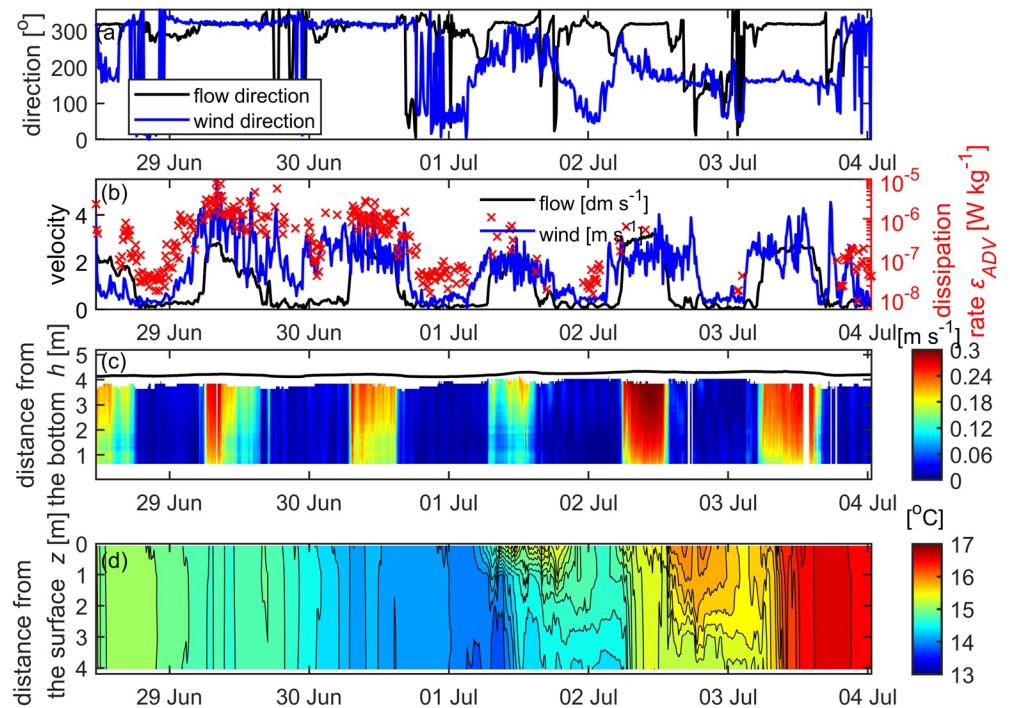


Figure 5. Time series of (a) flow direction (ADV, black line) and wind direction (blue line); (b) flow velocity (ADV [dm s^{-1}], black line), wind speed [m s^{-1}], blue line) and dissipation rate of turbulent kinetic energy (ADV, red crosses); (c) contours of flow velocity (ADCP), black line represents water surface; (d) water temperature. Data are from June 28 to July 04, 2018, emphasizing diel dynamics with a temporal resolution of 10 min.

is expected to be logarithmic (up to 0.6 of the water depth H). We did not find a good agreement between the mean ADCP dissipation rate profile and the two scaling relations for dissipation rates based on linearly decreasing shear stress toward the water surface (Equations 11 and 12). Both profiles agreed well with each other at a distance of 0.7 m above the bottom and deviated from the ADV dissipation rate at 0.4 m depth by a factor of 4 and 10, respectively. In contrast to the empirical approach by Nezu (1977), the model of Nikora and Smart (1996) converges to zero at the water surface (Figure 6a).

In contradiction to the scaling of vertical profiles of dissipation rates, the averaged Reynolds shear stress profile was not constant over depth, but closely followed a linear decrease toward zero at the water surface, as assumed in the derivation of Equations 11 and 12 (see, Figure S7 in Supporting Information S1).

The average value of the bottom drag coefficient at 1 m distance above the bed equaled to $C_{Dw} = 0.002$. For a water depth of 0.4 m we estimated a value of $C_{Dw} = 0.0015$. There was generally good agreement between bin-averaged near-surface dissipation rates estimated from the bed friction velocity derived from ADCP measurements (u_{*B}), and dissipation rates predicted from mean flow velocity measured by the ADV ($\epsilon_{BBL,ADV}$, Equation 13, see Figure 6b).

3.3. Turbulence Generated by Atmospheric Forcing

We examined the relation between dissipation and atmospheric forcing for cases when $\epsilon_{SBL} > \epsilon_{BBL}$. Bin-averaged rates of dissipation of turbulent kinetic energy predicted from bulk atmospheric forcing (ϵ_{SBL} , Equations 6 and 7) agreed reasonably well with dissipation rates estimated from ADV measurements (ϵ_{ADV}) over nearly three orders of magnitude (Figure 7a). The predicted values slightly underestimated dissipation rates in the higher range of the data. Considering only data for which the wind direction was along the river ($151^\circ \leq w_{dir} \leq 190^\circ$ and $290^\circ \leq w_{dir} \leq 323^\circ$) did not improve the agreement significantly (a two-sample Kolmogorov-Smirnov test showed no significant difference between them) (Figure 7b). The average ratio of predicted and observed dissipation rates was $\mu = 1.2$ in both cases.

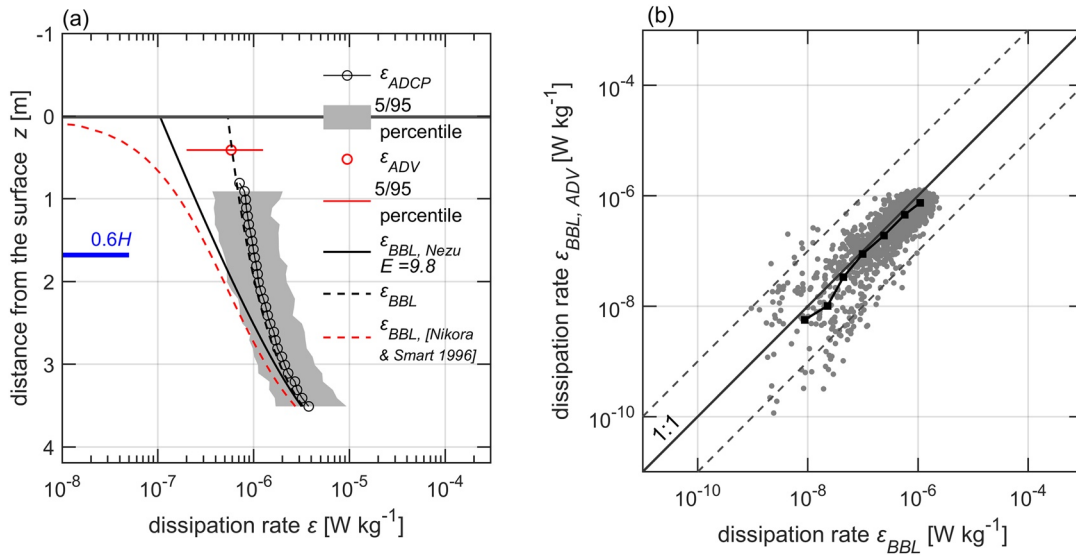


Figure 6. (a) Temporarily averaged dissipation rate profiles during conditions at which bed shear stress was expected to dominate turbulent dissipation near the water surface: the black line with open circles shows dissipation rates obtained by inertial subrange fitting from ADCP measurements (ϵ_{ADCP} , number of data points at 1 m distance above the bed: 53). The gray area marks the 5th to 95th percentile range of the data. The empty red circle shows the mean dissipation rate (and percentile range) estimated by inertial subrange fitting of ADV measurements (ϵ_{ADV}). The solid black line represents $\epsilon_{BBL, Nezu}$ (Equation 11), the dashed black line represents ϵ_{BBL} (Equation 10) and dashed red line represents $\epsilon_{BBL, NS}$ (Equation 12). For ϵ_{ADCP} we considered only those profiles which have at least 80% data in vertical direction and at least 20 time intervals. The thick horizontal line marks the water surface. The thick blue line corresponds to the depth up to which the logarithmic velocity law is valid (0.6 of water depth H). (b) Dissipation rates at 0.4 m water depth estimated from mean flow velocities measured by ADV ($\epsilon_{BBL, ADV}$, Equation 16) versus dissipation rates estimated from shear stresses obtained from ADCP data (ϵ_{BBL} , Equation 10). The black line with square symbols shows bin-averaged data. Number of data points in the plot is 1714. The solid gray line shows the 1:1 relationship and two dashed lines indicate differences of one order of magnitude.

Dissipation rates estimated from measured momentum fluxes by the EC system ($\epsilon_{SBL, EC}$, Equation 8) exceeded observed dissipation rates by a factor of five on average (Figure 8a). The large difference between the two dissipation rates estimated from atmospheric forcing were related to the difference between measured wind friction velocity and that estimated from mean wind speed in the bulk scaling (Figure 8b), with the latter

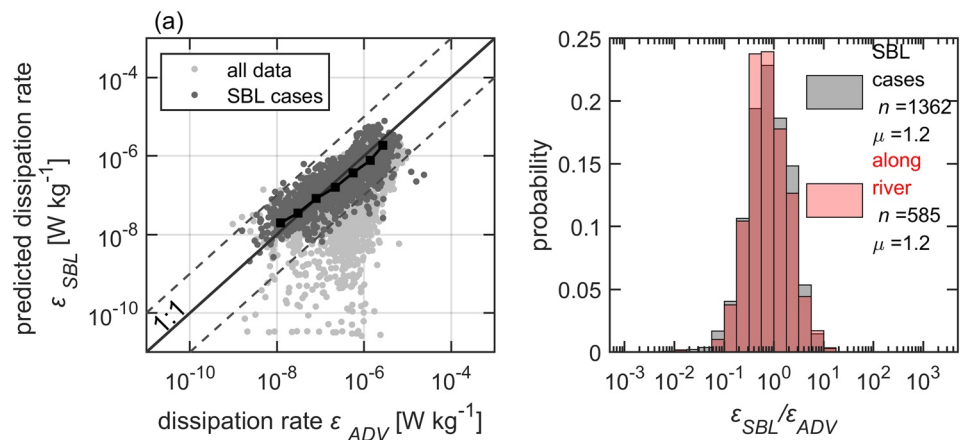


Figure 7. (a) Predicted dissipation rate of turbulent kinetic energy from bulk meteorological forcing ϵ_{SBL} versus observed dissipation rate ϵ_{ADV} at 0.4 m water depth. Light gray symbols show all data, dark gray symbols mark data for the selected cases for which near-surface turbulence was driven by atmospheric forcing (SBL cases). The black line with square symbols shows bin-averaged selected data. The solid gray line shows the 1:1 relation and two dashed lines indicate differences of one order of magnitude. (b) Probability distributions (bar graphs) of the ratio of ϵ_{SBL} and ϵ_{ADV} for all data with predominant atmospheric forcing (gray), and for the subset of this selection for which the wind directions were along the river ($151^\circ \leq w_{dir} \leq 190^\circ$ and $290^\circ \leq w_{dir} \leq 323^\circ$) (red). The number of data points n and the mean values μ of both distributions are provided in the legend.

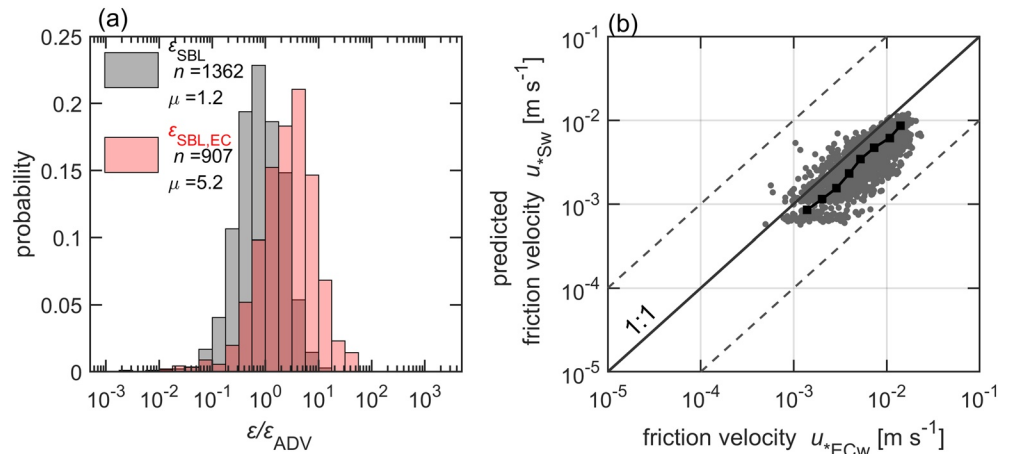


Figure 8. (a) Probability distributions (bar charts) of the ratio of dissipation rates estimated from atmospheric forcing and dissipation rates computed from measurements at 0.4 m depth. The gray bars show the distribution for bulk scaling (ϵ_{SBL} , Equations 6 and 7) and the red chart shows the ratio for dissipation rates estimated from measured momentum fluxes by the eddy covariance system ($\epsilon_{SBL,EC}$, Equation 8). Only selected data for periods when atmospheric forcing is expected to dominate near-surface turbulence are shown. The number of data points n and mean values of the ratio μ are shown in the legend. (b) Measured wind friction velocity by EC u_{*ECW} versus predicted friction velocity calculated from the bulk approach u_{*Sw} . The solid black line indicates a bin-average of the data, the gray solid line shows a 1:1 ratio and the two gray dashed lines represent one order of magnitude difference.

being consistently smaller than those derived from measurements. The agreement between the measured and predicted friction velocities was not improved if only wind directions along the river were considered.

We additionally tested a scaling relation for near-surface dissipation rates under breaking surface waves proposed for large lakes (Wang et al., 2013, 2015) (see Appendix A for details). We estimated the dissipation rate by taking measured significant wave height into account (see Appendix A, Figure S9a in Supporting Information S1). In comparison to dissipation rates predicted from bulk atmospheric forcing (ϵ_{SBL}), the wave scaling (ϵ_{wave}) did not improve the prediction quality (mean value of the ratio of ϵ_{wave} and ϵ_{ADV} $\mu = 0.1$, see, Figure S9b in Supporting Information S1). On average, ADV dissipation rates were a factor of 10 higher than the prediction ϵ_{wave} . The wave contribution to the dissipation rate was small due to much larger relative depth (depth of the dissipation rate measurements over the significant wave height) than in the former observations made in large lakes.

Table 4
Relative Contribution of Different Forcing Mechanisms to Near-Surface Dissipation Rates (0.4 m depth)

Dominance of:	Wind, buoyancy flux and mean flow	Wind and mean flow
$\epsilon_{SBL,wind}$	$n = 5564$ 44%	$n = 7199$ 60%
$\epsilon_{SBL,buoy}$	$n = 1839$ 15%	
ϵ_{BBL}	$n = 5081$ 40%	$n = 6266$ 40%
Total amount of data	$n = 12,646$ 100%	$n = 13,465$ 100%

Note. As an indicator for the dominating forcing mechanism, the first column shows the predicted dissipation with the maximum magnitude: ϵ_{SBL} , wind estimated from wind speed, ϵ_{SBL} , buoy estimated from buoyancy flux and ϵ_{BBL} estimated from mean flow velocity. n is a number of observations (10 min sampling intervals) and percentages refer to relative occurrence during the observational period. The second column shows the relative contributions of wind and mean flow velocity with disregarding the buoyancy flux.

3.4. Relative Importance of Atmospheric Forcing and Bottom-Generated Turbulence

To evaluate the relative contributions of different generation mechanisms to turbulence near the water surface, we classified all 10 min data segments throughout the observational period according to the highest values of predicted dissipation rates at 0.4 m water depth. For this analysis we used dissipation rates estimated from mean flow velocity observed by the ADV ($\epsilon_{BBL,ADV}$) and from bulk atmospheric forcing ($\epsilon_{SBL,wind}$, $\epsilon_{SBL,buoy}$). Conditions for which $\epsilon_{BBL,ADV}$ was larger than $\epsilon_{SBL,wind}$ and $\epsilon_{SBL,buoy}$, but smaller than their sum, were only 1% of total cases and are not included in further analyses.

Between June and September bottom-generated turbulence dominated for 40% of the time, wind 44%, and convective cooling 15% of the time (Table 4). Despite the large scatter of individual 10-min estimates, bin-averaged dissipation rates predicted from mean flow velocity and atmospheric forcing agree well with our observations ($\rho = 0.5$, $p < 0.05$,

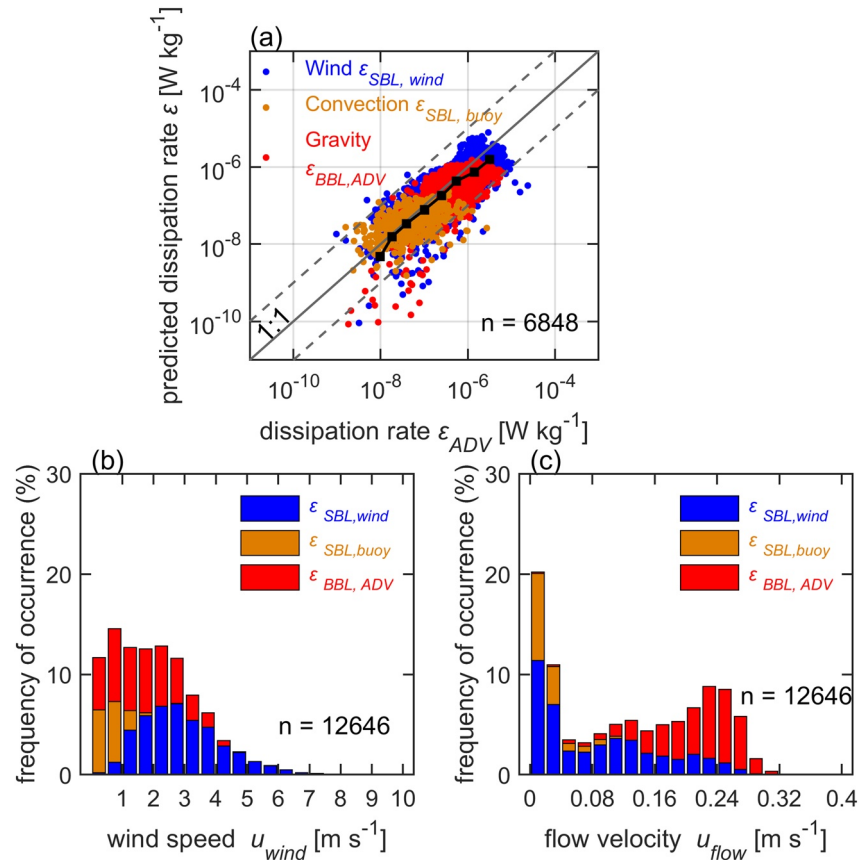


Figure 9. (a) Predicted dissipation rates of turbulent kinetic energy at 0.4 m water depth vs. observed values ϵ_{ADV} ($n = 6,848$ number of the data points resulted from the intersection of the ADV dissipation rate measurements (7,452) and combined predicted dissipation rate). Predictions are based on wind speed $\epsilon_{SBL,wind}$ and buoyancy flux $\epsilon_{SBL,buoy}$ if atmospheric forcing was the dominant driver of the near surface turbulence (blue and orange symbols, respectively). The predictions are based on bottom-boundary layer scaling estimated from mean flow velocity $\epsilon_{BBL,ADV}$ when the bottom-generated turbulence was dominant (red symbols). The dominant forcing mechanism was identified as the largest value of the three predictions. The black line with square symbols indicates bin-averaged data over all forcing conditions. The solid gray line shows a 1:1 relation, dashed lines represent a one order of magnitude difference. The symbols are partly overlapping, red and orange were plotted on top of blue. (b) Relative frequency of occurrence of dominant forcing conditions as a function of wind speed and (c) mean flow velocity. n indicates number of data points.

Figure 9a). The mean ratio of predicted and observed dissipation rates was 1.0. We additionally estimated the relative contributions of turbulence from wind speed and from gravity-generated flows, while disregarding buoyancy flux which is not always available in all studies. In this analysis we predicted the dissipation rate at 0.4 m water depth either from Equation 16 or (6), depending on which of both predictions was higher. The statistics of the dominant forcing mechanisms changed only slightly. Wind- and bottom-generated turbulence dominated in 53% and 47% of total time, respectively (Table 4).

Wind shear affected near-surface dissipation rates for wind speeds greater than 1 m s⁻¹ and was the dominant mechanism for wind speeds exceeding 3 m s⁻¹ (Figure 9b). When the flow velocity exceeded 9–10 cm s⁻¹, the bottom-generated turbulence dominated the near surface energy dissipation (Figure 9c). The contribution of the buoyancy flux was important at night, when the convective cooling coincided with low flow velocity and low wind speed. It was the most frequent cause of turbulence at wind speeds less than 2 m s⁻¹ and flow velocities less than 9–10 cm s⁻¹.

The effect of thermal stratification is not included in the scaling approaches that we used to estimate near-surface dissipation rates from bulk forcing variables. To test its importance, we comparing the probability distributions of the ratio of predicted and observed dissipation rates for cases with and without thermal stratification (temperature difference > 0.05°C). Except for periods of convective cooling, stratification

did not change the agreement between predictions and observations significantly (mean value of the ratio differed by less than 20%). In the rare case of convective turbulence in the presence of thermal stratification (3% of the observational period), the predictions based on buoyancy flux overestimated observed dissipation rates by 40% on average (Figure S10b in Supporting Information S1).

To test the effect of wind direction relative to the flow direction on near-surface dissipation rates, we separated the data into cases when the wind directions was along the longitudinal river flow direction ($290^\circ \leq w_{\text{dir}} \leq 323^\circ$) and against ($151^\circ \leq w_{\text{dir}} \leq 190^\circ$). Significant differences between predictions and observations were found between both cases, if wind or gravity was the dominant forcing mechanism (Figure S11 in Supporting Information S1). For wind-generated turbulence, the predictions underestimated near-surface dissipation rates by 10% for the periods when wind direction was along river flow in comparison to the periods when the wind direction was against the river flow. When bottom-generated turbulence was dominant, the predicted dissipation rates were lower than observed values by 10% and 20% for wind direction against and along the river, respectively.

3.5. Effect of Water Depth

To assess the extent to which dominant controls depend on water depth as well as on the distance below the surface, at which dissipation rates are evaluated, we calculated the ratio of dissipation rates resulting from bed friction (Equation 16) and from wind forcing (Equation 6). We derived a “critical” wind speed, for which both dissipation rates are equal, that is, for wind speeds greater than the critical wind speed, wind is the dominant forcing of near-surface turbulence:

$$u_{\text{wind crit}} = \bar{u}_{\text{flow}} \frac{1}{C_1} \left(\frac{\rho_w}{\rho_a} \right)^{\frac{1}{2}} \left(\frac{C_{Dw}}{C_{Da}} \right)^{\frac{1}{2}} \left(\frac{z}{H-z} \right)^{\frac{1}{3}}. \quad (17)$$

Note, that we did not consider the cases where buoyancy-driven turbulence dominated because we assumed its contribution was not significant in time. This equation is not accurate during stable density stratification (see Figure S10 in Supporting Information S1).

We calculated the critical wind speed $u_{\text{wind crit}}$ for the depth of 0.4 m using estimated for this depth the drag coefficient (ADV measurements). For the water depth at our sampling site of 4.2 m, $u_{\text{wind crit}}$ increased from 1 to 7.2 m s⁻¹ for mean flow velocities between 0.1 and 0.35 m s⁻¹. For a flow velocity of 0.35 m s⁻¹, the critical wind speed decreases from 13.4 m s⁻¹ for a flow depth of 1–2.4 m s⁻¹ for 100 m depth (Figure 10a).

The critical wind speed increases strongly with increasing depth at which wind and bottom-generated turbulence are compared. Using Equation 17, we computed the mean critical wind speed as a function sampling depth below the surface for the range of observed mean flow velocities (at 1 m above the river bed). At the ADV sampling depth (0.4 m below the surface), the mean critical wind is a factor of 6.8 higher compared to $u_{\text{wind crit}}$ estimated for a sampling depth of 1 mm below the surface. This depth corresponds to the Kolmogorov microscale of turbulence $L_k = (\nu^3/\epsilon)^{\frac{1}{4}}$, which defines the thickness of a viscous sublayer at the water surface and the depth at which turbulent energy dissipation rates are maximal (Lorke & Peeters, 2006). The value of the Kolmogorov microscale was calculated from the the log-averaged value of the observed dissipation rates at 0.4 m depth.

3.6. Verification of Equilibrium Between Production and Dissipation of TKE

We used the numerical 1D $k - \epsilon$ model to validate the assumption of local equilibrium between production and dissipation rates of turbulent kinetic energy (Equation 2). The model includes the effects of wind (excluding surface waves), river flow and vertical heat transport on turbulence throughout the water column. In general, results from the $k - \epsilon$ model showed good agreement with observed dissipation rates at 0.4 m water depth ($\rho = 0.5$, $p < 0.05$, Figure S12 in Supporting Information S1). However, there was a systematic difference at lower dissipation rates, for which the $k - \epsilon$ model underestimated the dissipation rates by up to a factor of 5–10 on average. On average, the model slightly underestimated the dissipation rate at 0.4 m water depth by 10% (Figure S12b in Supporting Information S1). The results of the model revealed that

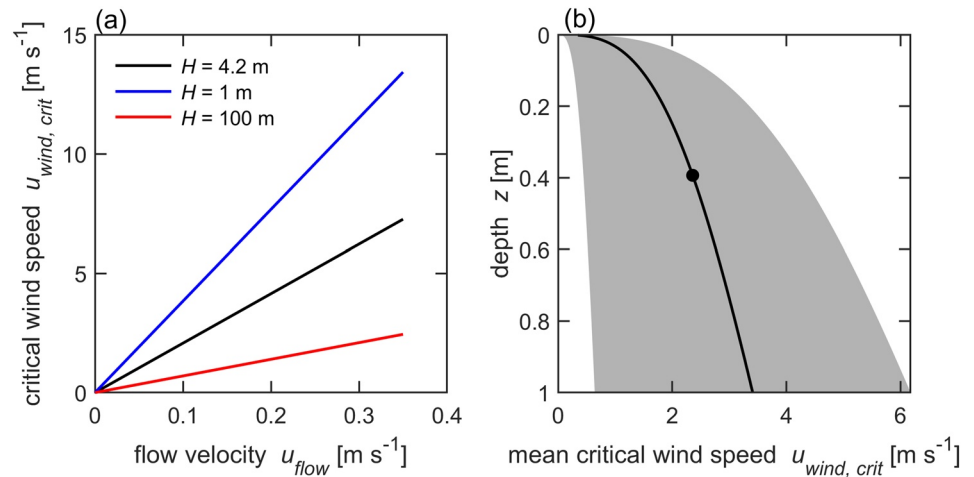


Figure 10. (a) Critical wind speed, above which near-surface turbulence is dominated by wind forcing (Equation 17 with the drag coefficient estimated for the depth of 0.4 m $C_{Dw} = 0.0015$) versus mean flow velocity for water depths H of 4.2 m (black line), 1 m (blue line), 100 m (red line). The depth at which wind- and bottom-generated dissipation rates are compared is 0.4 m (ADV sampling depth). (b) Vertical distribution of mean critical wind speed (black line) calculated for the mean flow velocity observed at 1 m above the bed. The drag coefficient corresponded to 1 m above the bed $C_{Dw} = 0.002$. The gray area encompasses the range of measured mean flow velocities (plus/minus one standard deviation). The black circle marks the depth of 0.4 m for which the critical wind speed in panel (a) was estimated. The uppermost depth corresponds to the lower edge of the viscous sublayer (equal to the mean Kolmogorov microscale of 1 mm).

TKE production was balanced by dissipation during most of the observational period. Only for 13% and 2% of the total data (1,463 and 166 10-min periods), turbulent transport of TKE (terms [2, 3] in Equation 1), and TKE tendency (term [1]) were larger than the sum of the production terms (terms [6,7]), respectively (Figure 11a). Disregarding data from time periods when the model predicted significant contributions of TKE transport or unsteadiness did not improve the agreement between dissipation rates obtained from measurements and from bulk forcing variables (Figure 11b). The mean value of the transport terms was

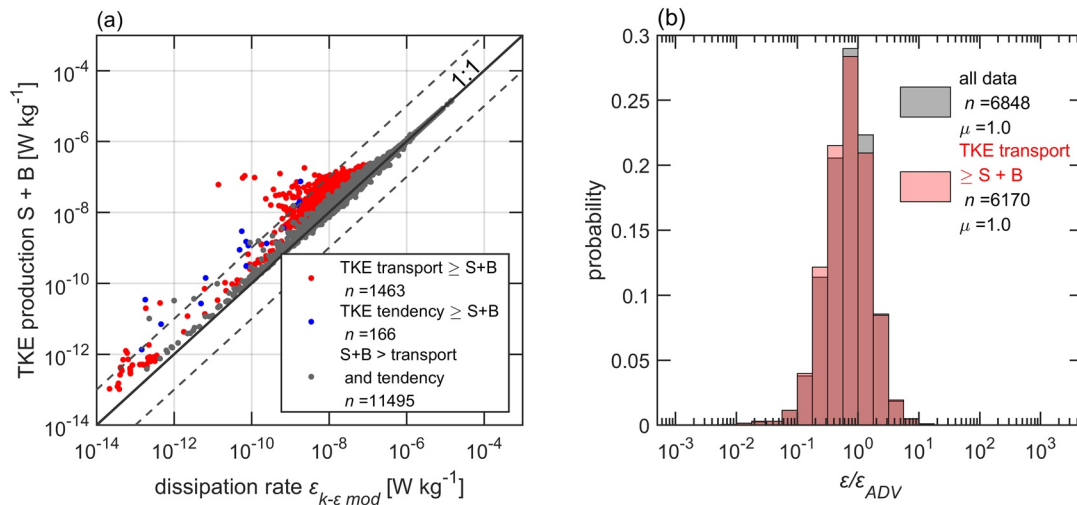


Figure 11. (a) Sum of production rates turbulent kinetic energy (TKE) by mean shear (S) and buoyancy flux (B) vs. TKE dissipation rates (Equation 1) simulated by the $k - \epsilon$ model. Gray dots (11,495 data points) show cases for which local TKE production rates was the dominant source of dissipated energy. Red and blue dots represent the cases when turbulent transport of TKE (1,463 data points) or TKE tendency (166 data points) exceeded the sum of the two production terms. (b) Probability distributions of the ratio of predicted and observed dissipation rates ϵ_{ADV} . Gray bars correspond to the ratio of the predicted dissipation rates from bulk approaches (ϵ_{SBL} , ϵ_{BBL}) and ϵ_{ADV} . Red bars show the same ratio but without the data for which TKE production and dissipation were not in balance (marked by blue or red color in [a]). The respective number of data points (n , also in [a]) and the mean value (μ) of the ratio are shown the legend.

equal to $4.3 \cdot 10^{-9} [\text{W kg}^{-1}]$, which was smaller than most of our measured dissipation rates (ϵ_{ADV} was less than this value only in 1% of the total number of measurements). These findings validate the assumption of a local equilibrium between TKE production and dissipation, which we made for inertial subrange fitting and bulk approaches.

Surface water temperature was slightly underestimated by the $k - \epsilon$ model, with a mean difference between modeled and observed temperature of -0.8°C (Figure S13 in Supporting Information S1). The inaccuracies in prediction of dissipation rate occurred when the water was stratified (Figure S12a in Supporting Information S1). The modeled flow velocity profile (Figure S14 in Supporting Information S1) was characterized by the patterns of flow regulation similar to what was observed.

4. Discussion

4.1. Magnitude, Drivers and Dynamics of Near-Surface Turbulence

Our measurements are the first to identify the dominant forcing mechanisms of near-surface turbulence in a large regulated river and their dynamics from minutes to seasonal time scales. Bed friction of gravity-driven flow and wind shear were nearly equally important forcing mechanisms and made dominant contributions to near-surface energy dissipation during 40% and 44% of the observational period, respectively. Convective cooling dominated energy dissipation rates only during 15% of the time. The temporal dynamics resulted from diel variability in wind speed, buoyancy flux and flow velocity. The latter was strongly affected by flow regulation. The nocturnal reduction of flow velocity due to demand-following hydropower production was frequently associated with a transition from the dominance of bottom-generated turbulence to atmospheric forcing and a change of the water body from a lotic to a more lentic-like system.

With a Strahler stream order of 5 and a width of approximately 100 m at the study site, the River Kitinen belongs to the class of moderately sized rivers (orders 5–9), which contribute the largest surface area globally, with less area covered by lower and higher order streams (Downing et al., 2012). Despite their widespread distribution, turbulence measurements in such rivers are rare. In the River Kitinen, dissipation rates of turbulent kinetic energy varied over five orders of magnitude 10^{-10} and $10^{-5} \text{ W kg}^{-1}$ during the ice-free season, with a log-averaged mean value of $4.2 \cdot 10^{-7} \text{ W kg}^{-1}$. This range is comparable to dissipation rates reported from shorter-term observations in a river of similar size in Germany (Lorke et al., 2012). In low-order streams, dissipation rates can be up to four orders of magnitude higher (Kokic et al., 2018), similar to tidal estuaries where dissipation estimates rates range from 10^{-6} – $10^{-4} \text{ W kg}^{-1}$ (Chickadel et al., 2011; Zappa et al., 2007). The comparably low dissipation rates in the River Kitinen were similar in magnitude to dissipation rates observed in the near-surface layer of lakes, where they typically vary between 10^{-9} and $10^{-5} \text{ W kg}^{-1}$ (Tedford et al., 2014; Wüest & Lorke, 2003).

Our study also showed that the contribution of surface waves to dissipation rates was insignificant, probably due to the small amplitude of the observed waves. Wind direction relative to the flow influenced dissipation rates only up to 10%, which is within the error of the measurements. Weak thermal stratification caused a slight suppression of turbulence. This result is in contrast to observations in a strongly stratified estuary, where wind was identified as the primary driver of near-surface turbulence. In these studies, turbulence from bed friction was attenuated by vertical density stratification caused by seawater intrusions (Orton, McGillis, & Zappa, 2010; Orton, Zappa, & McGillis, 2010).

4.2. Scaling and Modeling Near-Surface Turbulence

When atmospheric forcing dominated, near-surface dissipation rates followed a similarity scaling, as it been found in lakes and oceans (Lombardo & Gregg, 1989; Tedford et al., 2014) and could be well predicted from bulk parameters, including wind speed and surface buoyancy flux. Similarly, bottom-generated turbulence followed boundary-layer scaling and its vertical distribution could be well predicted from mean flow velocity after adjusting the bed roughness coefficient. Surprisingly, our observations showed that the vertical decline of bottom-generated turbulence was better described by the law-of-the-wall scaling, which is based on the assumption of a constant shear stress. This finding was in contrast to studies (Nezu, 1977; Nikora & Smart, 1996) in which empirical and theoretical approaches in open-channel flows are commonly applied.

The latter approaches have been found to agree well with vertical profiles of dissipation rates measured in smaller rivers (Sukhodolov et al., 1998) and in laboratory flumes (Johnson & Cowen, 2017; Nezu & Rodi, 1986). By combining both approaches for atmospheric and bottom-generated turbulence, we obtained a good prediction of near-surface dissipation rates as a function of bulk atmospheric forcing and mean flow velocity (Figure 9). Although the scatter of individual (10-min based) dissipation rates is large, bin-averaged data revealed an unbiased agreement between prediction and observation.

To assess the relative importance of bottom- and wind generated turbulence in rivers of arbitrary depth, we defined a critical wind speed, derived with the assumption that at some depth the surface boundary-induced turbulence is equal to the bottom boundary-induced turbulence. We combined both boundary-layer scaling approaches and derived an expression for the critical wind speed as a function of mean flow velocity and water depth (Equation 17). For wind speeds exceeding this critical value, near-surface turbulence is expected to be controlled by wind, in contrast to the predominance of bed friction for wind speed below the critical value.

In addition to bulk forcing and water depth, the relative importance of wind and bottom-generated turbulence depends strongly on the distance from the surface at which turbulence is observed. Particularly, wind-generated turbulence declines below the water surface and dissipation rates are expected to be highest at the base of the viscous sublayer at the water surface (Lorke & Peeters, 2006). As in most field observations of near-surface turbulence, the distance below the water surface at which turbulence was observed (0.4 m) was limited by the physical dimension of the velocimeter. Spatially resolving measurements of turbulence in the wind-mixed surface layer of a lake using particle image velocimetry, confirmed the existence of a power-law decline of dissipation rates, even within the uppermost centimeter of the water column (Wang et al., 2013). The relative importance of wind or flow generated turbulence can be estimated as a function of distance from the water surface using law-of-the-wall scaling (Equation 17).

A 1D $k - \epsilon$ model for rivers has been applied to quantify the turbulence throughout the water column. Despite the higher numerical complexity and more comprehensive physics compared to bulk approaches, the $k - \epsilon$ model results did not demonstrate substantial improvement in simulating subsurface dissipation rates compared to the similarity-based estimates. The model results were comparable to surface similarity scaling when the atmospheric forcing was dominant, because the top boundary condition used in the model is of the same type as that used in the scaling. When the turbulence was dominated by bed friction, the $k - \epsilon$ model slightly underestimated the dissipation rates. This result should be interpreted with caution, since the dissipation rate measurements contain significant uncertainties themselves (discussed below). The discrepancies may also result from the well-known knowledge gaps in the construction of optimal two-parameter (e.g., $k - \epsilon$) turbulence closures, namely, specification of stability functions and non-dimensional constants (Mortikov et al., 2019), setup of the surface boundary conditions (Burchard, 2002), and inclusion of TKE production by wave-induced motions (Ghantous & Babanin, 2014), to mention a few. This study also indicates, that model improvements will need to address the overestimation of solar heating below the water column top (and corresponding diminishing of turbulence) under low wind and flow speed conditions.

4.3. Uncertainties in Dissipation Rate Estimates

The unique longer-term observations of near-surface TKE dissipation rates were obtained by invoking a number of rigorous assumptions and simplifications. The most complete data set was obtained from the ADV observations at a fixed depth of 0.4 m below the water surface. While we aimed at estimating dissipation rates in close proximity to the water surface, the sampling depth of the ADV was limited by deployment considerations, which ensured that the transducer head remained submerged below the water surface also in the presence of wind-generated waves. The ADCP measurements provided support for choosing a relationship describing the vertical profile of turbulence generated by bed friction, although the sampling volume of the ADCP was three orders of magnitude larger than that of the ADV. This limitation, an addition to the undetermined isotropy constant for the radial along-beam velocities (Lorke & Wüest, 2005), made the ADCP measurements less favorable for estimating dissipation rates near the water surface.

Dissipation rates were estimated from measured flow velocities and bulk scaling approaches by assuming a simplified balance of turbulent kinetic energy, in which production and dissipation are in equilibrium.

In studies of bottom-generated turbulence in rivers with high flow speeds this assumption is challenged by theoretical considerations (Nezu & Nakagawa, 1993) and by observations (Scully et al., 2011; Talke et al., 2013). In these cases, energy dissipation rates near the water surface exceeded local production rates and were balanced by upward transport of TKE from the near-bed region. We tested whether such vertical transport would occur for the flow conditions in the Kitinen River using the $k - \epsilon$ model. Results indicated that TKE transport and unsteadiness of the TKE balance (TKE tendency) were small compared to TKE production near the surface by shear and buoyancy flux and the near-equal dissipation rates. This finding was true for 85% of the observational period. Disregarding observations from the brief periods when the simulations showed significant contributions from turbulent transport and TKE tendency did not improve the predictions based on bulk approaches (Figure 11).

Our results differ from those in the more energetic tidal rivers. In these, dissipation rates were about two orders of magnitude higher than in the Kitinen River and vertical TKE flux divergence was observed (Scully et al., 2011; Talke et al., 2013). At these energetic sites, coherent flow structures enhanced TKE transport from the river bed to the surface (Talke et al., 2013). Such coherent structures, or boils, consist of localized upwelling motions which constantly disrupt the water surface. While these structures cannot be resolved by the one-dimensional $k - \epsilon$ model, energetic boils were not observed visually in our velocity measurements. TKE divergence due to larger-scale vertical motions would not affect the presence of an inertial subrange in spectra of near-surface velocity fluctuations (Flores et al., 2017; Scully et al., 2011; Talke et al., 2013). However, bulk scaling approaches relying on the law-of-the-wall would not apply (Equations 10 and 12), which is in contrary to our observations.

The validity of our estimates of dissipation rates also requires that the turbulence be isotropic over the range in which we did our calculation. In energetic river flows, anisotropy has been found near the water surface where vertical velocity fluctuations can be suppressed. However, both observations (Talke et al., 2013) and direct numerical simulations (Flores et al., 2017) show that an inertial subrange, exists for the horizontal velocity components near the free water surface. Within an integral length (corresponding to the distance from the boundary), the flow has adjusted to isotropic turbulence and dissipation rates can be obtained from vertical velocity fluctuations using the inertial dissipation method. We validated that the flow was isotropic based on comparisons of dissipation rates of the three components of velocity when the noise in the horizontal velocities was low enough for the measurement to be conducted (Figure S3 in Supporting Information S1). By bounding the lower limit of the wave number range that we used for inertial subrange fitting by that corresponding to the ADV sampling depth (0.4 m), we excluded the larger anisotropic scales. The vertical velocity component was used in analysis due to its lower noise.

Estimates of dissipation rates using the inertial dissipation method have been found to be in good agreement with those obtained from other estimation techniques (e.g., the structure function method McMillan & Hay, 2017, temperature microstructure measurements Lorke & Wüest, 2005 and direct dissipation estimates from particle image velocimetry Wang et al., 2013), over a wide range of boundary-layer flows. The cumulative uncertainties in the measurement related to dissipation rates has been estimated to be within a factor of two (Moum et al., 1995). Bin-averaged dissipation rates predicted using bulk scaling approaches generally agreed with the measurements within a factor of two (e.g., Figures 6b, 7a and 9a). For further understanding of processes affecting near-surface dissipation rate in regulated rivers, future studies should include measurements to resolve additional components of the TKE budget (such as in Talke et al., 2013), and explore the application of optical remote sensing of surface flow structures for improved identification of coherent structures (Branch et al., 2021).

4.4. Implications for Gas Exchange in Regulated Rivers

Near-surface turbulence constitutes the primary control on the gas transfer velocity (k_g) at the air-water interface (MacIntyre et al., 2010; Zappa et al., 2007). k_g is related to the dissipation rate of turbulent kinetic energy as $k_g = c_1(\epsilon\nu)^{1/4}Sc^{-1/2}$, where Sc is a Schmidt number, c_1 is a scaling parameter (Lamont & Scott, 1970). The mean observed dissipation rate of $4.2 \cdot 10^{-7} \text{ W kg}^{-1}$ corresponds to the normalized value of k_{600} (i.e., for $Sc = 600$) of 1.5 m d^{-1} (using $c_1 = 0.5$ MacIntyre et al., 2010). This gas transfer velocity is approximately 4 times lower than what has been used for a river with Strahler order of 5 in a global analysis of inland water CO_2 emissions (Raymond et al., 2013). Moreover, the range of variability of dissipation rates

spanned four orders of magnitude, which corresponds to temporal variations in k_g of one order of magnitude ($0.3\text{--}4\text{ m d}^{-1}$), with most of the variability occurring at a diel time scale. As dissolved gas concentrations also often show diel variations in response to light and temperature, the diel variability of gas fluxes to the atmosphere can be amplified or attenuated, depending on the superposition of both cycles. To the best of our knowledge, direct measurements of gas fluxes from rivers using floating chamber or tracer methods have been conducted during daytime, which can potentially result in a significant bias if these fluxes are assumed to present daily or longer-term mean values in larger-scale estimates. To date, temporal variability of the gas transfer velocity has not been resolved in larger-scale models of riverine CO_2 emissions, where the gas transfer velocity is typically considered as constant for a stream segment or reach (Magin et al., 2017; Raymond et al., 2013; Lauerwald et al., 2015). Future field observations and modeling efforts are required to analyze the extent to which diel variability may affect longer-term emission rates.

Alin et al., (2011) suggested a conceptual scheme for the transition of the physical control of gas transfer velocities and fluxes in river systems from the dominance of wind control in estuaries and large rivers toward increasing importance of water current velocity and depth at progressively lower stream orders. Our findings confirm this scheme, with the Kitinen River being located in the transition zone, where wind and water currents are of nearly equal importance. Moreover, we provide a quantitative evaluation of this concept, by combining scaling relations for energy dissipation rates generated by wind and water currents as a function of river depth. Our concept of a critical wind speed can be used to separate the two physical forcing regimes and to estimate near-surface dissipation rates and corresponding gas transfer velocities from mean flow velocity or from wind speed.

The temporal dynamics of the near-surface turbulence were strongly affected by flow regulation. Demand-following hydropower generation resulted in diel changes of flow velocity from $0.2\text{--}0.3\text{ m s}^{-1}$ during daytime to some mm s^{-1} at night, changing the physical characteristics of the river from lotic to lentic. As the majority of river systems are affected by flow regulation (Grill et al., 2019), this situation can probably be considered as typical. Flow regulation has been shown to decrease flow variability at seasonal scales by homogenization of river discharge (Poff et al., 2007; Long et al., 2019). The effect of flow regulation on shorter, including diel time scales has received comparably less attention. In the regulated river Saar in central Europe, diel variations in flow velocity have been shown to modulate the oxygen flux into the river bed by a factor of two (Lorke et al., 2012). The availability of oxygen in river sediment can be expected to affect mineralization rates and the production of greenhouse gases. Therefore, flow regulation not only modulates near-surface turbulence and, therewith the temporal dynamics of gas fluxes, it may additionally affect the total amount of greenhouse gases emitted from rivers. Despite its global relevance, this potential implication has not been explored and should be addressed in future studies. Such studies can be based on the scaling approaches or on the 1D $k - \epsilon$ model, which can be combined with biogeochemical models for water and sediment as has also been done for lakes at regional scales (e.g., Sabrekov et al., 2017). These models can be used to explore and to optimize management strategies for flow regulation, that can potentially mitigate adverse effects of river damming on greenhouse gas emissions.

5. Conclusion

Our study provides the first continuous turbulence measurements in a large regulated river. We found nearly equal contributions from atmospheric forcing and bottom-generated turbulence to near-surface dissipation rates with wind being the dominant driver for wind speeds exceeding 3 m s^{-1} , and bottom-generated shear when flow speeds exceeded $0.09\text{--}0.1\text{ m s}^{-1}$. After validation of individual scaling approaches, we developed a scaling approach to quantify the dominant forcing mechanism (wind or flow) using a critical value of the wind speed, which depends on mean flow velocity and flow depth. As flow regulation proved to be important for the temporal dynamics of the near-surface turbulence, future studies should address the implications of daily and sub-daily flow variations on both the temporal dynamics of fluxes and biogeochemical cycling in such rivers.

Appendix A: Wave-Breaking Scaling

Based on measurements in large lakes and in the coastal ocean, Terray et al. (1996); Feddersen et al. (2007) proposed the following scaling for near-surface dissipation rates under breaking surface waves in deep water:

$$\frac{\epsilon_{\text{wave}} H_{\text{sign}}}{\alpha(u_{*Sw})^3} = \beta \left(\frac{z}{H_{\text{sign}}} \right)^m, \quad (\text{A1})$$

where z is the distance from the water surface, H_{sign} is the significant wave height, $\alpha \sim c_p/u_{*Sw}$ (where c_p is the wave phase speed) is a coefficient which has been found in (Feddersen et al., 2007) equal to 250 for the coastal ocean, $\beta = 0.3$ and $m = -2$ are the constants. However, measurements conducted by (Wang et al., 2013, 2015) in a large lake suggested scaling constants of $\beta = 0.04$, $m = -0.73$ within the top layer of water column.

We obtained α and m using a linear regression model for filtered data with wind speed exceeding 1 m s^{-1} and wind directions along the river (see Figure S9a in Supporting Information S1). The friction velocity u_{*Sw} was calculated from mean wind speed. We found $\alpha = 54$ and $m = -0.9$ which were close to the result in (Wang et al., 2013, 2015). With these values we estimated the dissipation rate including the effect of waves ϵ_{wave} using Equation A2:

$$\epsilon_{\text{wave}} = \beta \alpha (u_{*Sw})^3 \frac{H_{\text{sign}}}{z^2}. \quad (\text{A2})$$

Conflict of Interest

The authors declare no conflicts of interest relevant to this study.

Data Availability Statement

The data used in this study is available at the Mendeley repository Guseva et al., 2020 [doi: 10.17632/jnbx-wyybcn.2]. We are grateful for the scripts provided by Cynthia Bluteau and Galen Charles Egan.

References

- Åberg, S. C., Korkka-Niemi, K., Rautio, A., Salonen, V.-P., & Åberg, A. K. (2019). Groundwater recharge/discharge patterns and groundwater-surface water interactions in a sedimentary aquifer along the River Kitinen in Sodankylä, northern Finland. *Boreal Environment Research*, 24, 155–187.
- Alin, S. R., de Fátima Raseira, F. L. M., Salimon, C. I., Richey, J. E., Holtgrieve, G. W., Krusche, A. V., & Snidvongs, A. (2011). Physical controls on carbon dioxide transfer velocity and flux in low-gradient river systems and implications for regional carbon budgets. *Journal of Geophysical Research: Biogeosciences*, 116(G1). <https://doi.org/10.1029/2010JG001398>
- Arcement, G. J., & Schneider, V. R. (1989). *Guide for selecting Manning's roughness coefficients for natural channels and flood plains*. US Government Printing Office.
- Aufdenkampe, A. K., Mayorga, E., Raymond, P. A., Melack, J. M., Doney, S. C., Alin, S. R., et al. (2011). Riverine coupling of biogeochemical cycles between land, oceans, and atmosphere. *Frontiers in Ecology and the Environment*, 9(1), 53–60. <https://doi.org/10.1890/100014>
- Baker, M. A., & Gibson, C. H. (1987). Sampling turbulence in the stratified ocean: Statistical Consequences of strong intermittency. *Journal of Physical Oceanography*, 17(10), 1817–1836. [https://doi.org/10.1175/1520-0485\(1987\)017<1817:stiso>2.0.co;2](https://doi.org/10.1175/1520-0485(1987)017<1817:stiso>2.0.co;2)
- Bluteau, C. E., Jones, N. L., & Ivey, G. N. (2011). Estimating turbulent kinetic energy dissipation using the inertial subrange method in environmental flows. *Limnology and Oceanography: Methods*, 9(7), 302–321. <https://doi.org/10.4319/lom.2011.9.302>
- Borges, A. V., Darchambeau, F., Teodoru, C. R., Marwick, T. R., Tamoo, F., Geeraert, N., et al. (2015). Globally significant greenhouse-gas emissions from African inland waters. *Nature Geoscience*, 8(8), 637–642. <https://doi.org/10.1038/ngeo2486>
- Bormans, M., & Webster, I. T. (1997). A mixing criterion for turbid rivers. *Environmental Modelling & Software*, 12(4), 329–333. [https://doi.org/10.1016/S1364-8152\(97\)00032-7](https://doi.org/10.1016/S1364-8152(97)00032-7)
- Bouffard, D., & Wüest, A. (2019). Convection in lakes. *Annual Review of Fluid Mechanics*, 51, 189–215. <https://doi.org/10.1146/annurev-fluid-010518-040506>
- Branch, R., Horner-Devine, A. R., Chickadel, C. C., Talke, S. A., Clark, D., & Jessup, A. (2021). Surface turbulence reveals riverbed drag coefficient. *Geophysical Research Letters*, 48(10), e2020GL092326. <https://doi.org/10.1029/2020GL092326>
- Brumer, S. E., Zappa, C. J., Blomquist, B. W., Fairall, C. W., Cifuentes-Lorenzen, A., Edson, J. B., et al. (2017). Wave-related Reynolds number parameterizations of CO₂ and DMS transfer velocities. *Geophysical Research Letters*, 44(19), 9865–9875. <https://doi.org/10.1002/2017GL074979>
- Burchard, H. (2002). *Applied turbulence modelling in marine waters* (Vol. 100). Springer Science & Business Media. <https://doi.org/10.1007/3-540-45419-5>

- Butman, D., & Raymond, P. A. (2011). Significant efflux of carbon dioxide from streams and rivers in the United States. *Nature Geoscience*, 4(12), 839–842. <https://doi.org/10.1038/ngeo1294>
- Cannon, D. J., & Troy, C. D. (2018). Observations of turbulence and mean flow in the low-energy hypolimnetic boundary layer of a large lake. *Limnology and Oceanography*, 63(6), 2762–2776. <https://doi.org/10.1002/lno.11007>
- Chickadel, C. C., Talke, S. A., Horner-Devine, A. R., & Jessup, A. T. (2011). Infrared-based measurements of velocity, turbulent kinetic energy, and dissipation at the water surface in a tidal river. *IEEE Geoscience and Remote Sensing Letters*, 8(5), 849–853. <https://doi.org/10.1109/LGRS.2011.2125942>
- Chow, V. T. (1959). *Open-channel hydraulics*. McGraw-Hill Book Co.
- Cole, J. J., Prairie, Y. T., Caraco, N. F., McDowell, W. H., Tranvik, L. J., Striegl, R. G., et al. (2007). Plumbing the global carbon cycle: Integrating inland waters into the terrestrial carbon budget. *Ecosystems*, 10(1), 172–185. <https://doi.org/10.1007/s10021-006-9013-8>
- Downing, J. A., Cole, J. J., Duarte, C., Middelburg, J. J., Melack, J. M., Prairie, Y. T., et al. (2012). Global abundance and size distribution of streams and rivers. *Inland Waters*, 2(4), 229–236. <https://doi.org/10.5268/IW-2.4.502>
- Feddersen, F., Trowbridge, J. H., & Williams, A., III. (2007). Vertical structure of dissipation in the nearshore. *Journal of Physical Oceanography*, 37(7), 1764–1777. <https://doi.org/10.1175/JPO3098.1>
- Flores, O., Riley, J. J., & Horner-Devine, A. R. (2017). On the dynamics of turbulence near a free surface. *Journal of Fluid Mechanics*, 821, 248–265. <https://doi.org/10.1017/jfm.2017.209>
- Foken, T. (2008). *Micrometeorology* (1st ed.). Springer, Berlin, Heidelberg. <https://doi.org/10.1007/978-3-540-74666-9>
- Gerbi, G. P., Trowbridge, J. H., Terray, E. A., Plueddemann, A. J., & Kukulka, T. (2009). Observations of turbulence in the ocean surface boundary layer: Energetics and transport. *Journal of Physical Oceanography*, 39(5), 1077–1096. <https://doi.org/10.1175/2008JPO4044.1>
- Ghantous, M., & Babanin, A. (2014). One-dimensional modelling of upper ocean mixing by turbulence due to wave orbital motion. *Non-linear Processes in Geophysics*, 21(1), 325–338. <https://doi.org/10.5194/npg-21-325-2014>
- Goring, D. G., & Nikora, V. I. (2002). Despiking acoustic doppler velocimeter data. *Journal of Hydraulic Engineering*, 128(1), 117–126. [https://doi.org/10.1061/\(asce\)0733-9429\(2002\)128:1\(117\)](https://doi.org/10.1061/(asce)0733-9429(2002)128:1(117))
- Grill, G., Lehner, B., Thieme, M., Geenen, B., Tickner, D., Antonelli, F., et al. (2019). Mapping the world's free-flowing rivers. *Nature*, 569(7755), 215–221. <https://doi.org/10.1038/s41586-019-1111-9>
- Guerra, M., & Thomson, J. (2017). Turbulence measurements from five-beam acoustic Doppler current profilers. *Journal of Atmospheric and Oceanic Technology*, 34(6), 1267–1284. <https://doi.org/10.1175/JTECH-D-16-0148.1>
- Hicks, B. (1972). Some evaluations of drag and bulk transfer coefficients over water bodies of different sizes. *Boundary-Layer Meteorology*, 3(2), 201–213. <https://doi.org/10.1007/BF02033919>
- Imberger, J. (1985). The diurnal mixed layer. *Limnology and oceanography*, 30(4), 737–770. <https://doi.org/10.4319/lo.1985.30.4.0737>
- Jabbari, A., Boegman, L., Valipour, R., Wain, D., & Bouffard, D. (2020). Dissipation of turbulent kinetic energy in the oscillating bottom boundary layer of a large shallow lake. *Journal of Atmospheric and Oceanic Technology*, 37(3), 517–531. <https://doi.org/10.1175/JTECH-D-19-0083.1>
- Johnson, E. D., & Cowen, E. A. (2017). Estimating bed shear stress from remotely measured surface turbulent dissipation fields in open channel flows. *Water Resources Research*, 53(3), 1982–1996. <https://doi.org/10.1002/2016WR018898>
- Katul, G., & Liu, H. (2017). Multiple mechanisms generate a universal scaling with dissipation for the air-water gas transfer velocity. *Geophysical Research Letters*, 44(4), 1892–1898. <https://doi.org/10.1002/2016GL072256>
- Kokic, J., Sahlée, E., Sobek, S., Vachon, D., & Wallin, M. B. (2018). High spatial variability of gas transfer velocity in streams revealed by turbulence measurements. *Inland Waters*, 8(4), 461–473. <https://doi.org/10.1080/20442041.2018.1500228>
- Krause, F. (2011). River management. Technological challenge or conceptual illusion? Salmon weirs and hydroelectric dams on the Kemi River in Northern Finland. In *Implementing environmental and resource management* (pp. 229–248). Springer. https://doi.org/10.1007/978-3-540-77568-3_19
- Kundu, P. K., Cohen, I., & Dowling, D. (2010). *Fluid mechanics* (4th ed.). Academic Press.
- Lamont, J. C., & Scott, D. (1970). An eddy cell model of mass transfer into the surface of a turbulent liquid. *AIChE Journal*, 16(4), 513–519. <https://doi.org/10.1002/aic.690160403>
- Lauerwald, R., Laruelle, G. G., Hartmann, J., Ciais, P., & Regnier, P. A. (2015). Spatial patterns in CO₂ evasion from the global river network. *Global Biogeochemical Cycles*, 29(5), 534–554. <https://doi.org/10.1002/2014GB004941>
- Lehner, B., Verdin, K., & Jarvis, A. (2008). New global hydrography derived from spaceborne elevation data. *Eos, Transactions American Geophysical Union*, 89(10), 93–94. <https://doi.org/10.1029/2008EO10001>
- Lombardo, C. P., & Gregg, M. C. (1989). Similarity scaling of viscous and thermal dissipation in a convecting surface boundary layer. *Journal of Geophysical Research: Oceans*, 94(C5), 6273–6284. <https://doi.org/10.1029/JC094iC05p06273>
- Long, L., Ji, D., Liu, D., Yang, Z., & Lorke, A. (2019). Effect of cascading reservoirs on the flow variation and thermal regime in the lower reaches of the Jinsha River. *Water*, 11(5), 1008. <https://doi.org/10.3390/w11051008>
- Lorke, A., & MacIntyre, S. (2009). The benthic boundary layer (in rivers, lakes, and reservoirs). In G. E. Likens (Ed.), *Encyclopedia of inland waters* (pp. 505–514): Academic Press. <https://doi.org/10.1016/B978-012370626-3.00079-X>
- Lorke, A., McGinnis, D. F., Maeck, A., & Fischer, H. (2012). Effect of ship locking on sediment oxygen uptake in impounded rivers. *Water Resources Research*, 48(12). <https://doi.org/10.1029/2012WR012483>
- Lorke, A., & Peeters, F. (2006). Toward a Unified Scaling Relation for Interfacial Fluxes. *Journal of Physical Oceanography*, 36(5), 955–961. <https://doi.org/10.1175/JPO2903.1>
- Lorke, A., & Wüest, A. (2005). Application of coherent ADCP for turbulence measurements in the bottom boundary layer. *Journal of Atmospheric and Oceanic Technology*, 22(11), 1821–1828. <https://doi.org/10.1175/JTECH1813.1>
- MacIntyre, S., Bastviken, D., Arneborg, L., Crowe, A. T., Karlsson, J., Andersson, A., et al. (2020). Turbulence in a small boreal lake: Consequences for air–water gas exchange. *Limnology and Oceanography*, 66(3), 827–854. <https://doi.org/10.1002/lno.11645>
- MacIntyre, S., Crowe, A. T., Cortés, A., & Arneborg, L. (2018). Turbulence in a small arctic pond. *Limnology and Oceanography*, 63(6), 2337–2358. <https://doi.org/10.1002/lno.10941>
- MacIntyre, S., Jonsson, A., Jansson, M., Aberg, J., Turney, D. E., & Miller, S. D. (2010). Buoyancy flux, turbulence, and the gas transfer coefficient in a stratified lake. *Geophysical Research Letters*, 37(24). <https://doi.org/10.1029/2010GL044164>
- MacIntyre, S., Romero, J. R., & Kling, G. W. (2002). Spatial-temporal variability in surface layer deepening and lateral advection in an embayment of Lake Victoria, East Africa. *Limnology and Oceanography*, 47(3), 656–671. <https://doi.org/10.4319/lo.2002.47.3.0656>
- MacIntyre, S., Romero, J. R., Silsbe, G. M., & Emery, B. M. (2014). Stratification and horizontal exchange in Lake Victoria, East Africa. *Limnology and Oceanography*, 59(6), 1805–1838. <https://doi.org/10.4319/lo.2014.59.6.1805>

- Magin, K., Somlai-Haase, C., Schäfer, R. B., & Lorke, A. (2017). Regional-scale lateral carbon transport and CO₂ evasion in temperate stream catchments. *Biogeosciences*, *14*(21), 5003–5014. <https://doi.org/10.5194/bg-14-5003-2017>
- McCaffrey, K., Fox-Kemper, B., Hamlington, P. E., & Thomson, J. (2015). Characterization of turbulence anisotropy, coherence, and intermittency at a prospective tidal energy site: Observational data analysis. *Renewable Energy*, *76*, 441–453. <https://doi.org/10.1016/j.renene.2014.11.063>
- McMillan, J. M., & Hay, A. E. (2017). Spectral and structure function estimates of turbulence dissipation rates in a high-flow tidal channel using broadband ADCPs. *Journal of Atmospheric and Oceanic Technology*, *34*(1), 5–20. <https://doi.org/10.1175/JTECH-D-16-0131.1>
- McMillen, R. T. (1988). An eddy correlation technique with extended applicability to non-simple terrain. *Boundary-Layer Meteorology*, *43*(3), 231–245. <https://doi.org/10.1007/BF00128405>
- Mortikov, E., Glazunov, A., Debolskiy, A., Lykosov, V., & Zilitinkevich, S. (2019). Modeling of the dissipation rate of turbulent kinetic energy. *Doklady Earth Sciences*, *489*(2), 1440–1443. <https://doi.org/10.1134/S1028334X19120067>
- Moum, J. N., Gregg, M. C., Lien, R. C., & Carr, M. E. (1995). Comparison of turbulence kinetic energy dissipation rate estimates from two ocean microstructure profilers. *Journal of Atmospheric and Oceanic Technology*, *12*(2), 346–366. [https://doi.org/10.1175/1520-0426\(1995\)012<0346:cotked>2.0.co;2](https://doi.org/10.1175/1520-0426(1995)012<0346:cotked>2.0.co;2)
- Natchimuthu, S., Wallin, M. B., Klemedtsson, L., & Bastviken, D. (2017). Spatio-temporal patterns of stream methane and carbon dioxide emissions in a hemiboreal catchment in Southwest Sweden. *Scientific Reports*, *7*, 39729. <https://doi.org/10.1038/srep39729>
- Neumann, G., & Pierson, W. (1966). *Principles of physical oceanography*. Prentice-Hall.
- Nezu, I. (1977). *Turbulent structure in open-channel flows* (PhD dissertation). Kyoto University.
- Nezu, I., & Nakagawa, H. (1993). *Turbulence in open-channel flows* (pp. 281). IAHR Monograph.
- Nezu, I., & Rodi, W. (1986). Open-channel flow measurements with a laser Doppler anemometer. *Journal of Hydraulic Engineering*, *112*(5), 335–355. [https://doi.org/10.1061/\(asce\)0733-9429\(1986\)112:5\(335\)](https://doi.org/10.1061/(asce)0733-9429(1986)112:5(335))
- Nikora, V., & Roy, A. G. (2012). Secondary flows in rivers: Theoretical framework, recent advances, and current challenges. *Gravel bed rivers: Processes, tools, environments*. (3–22). Wiley Online Library.
- Nikora, V., & Smart, G. (1996). A simple model of turbulence intensity and turbulence scale distribution in gravel bed rivers. In *Advances in turbulence VI* (pp. 171–174). Springer. https://doi.org/10.1007/978-94-009-0297-8_47
- Nortek, A. S. (2015). *The comprehensive manual [computer software manual]*. Retrieved from <http://www.nortek.no/en/support/manuals>
- Orton, P. M., McGillis, W. R., & Zappa, C. J. (2010). Sea breeze forcing of estuary turbulence and air-water CO₂ exchange. *Geophysical Research Letters*, *37*(13). <https://doi.org/10.1029/2010GL043159>
- Orton, P. M., Zappa, C. J., & McGillis, W. R. (2010). Tidal and atmospheric influences on near-surface turbulence in an estuary. *Journal of Geophysical Research: Oceans*, *115*(C12). <https://doi.org/10.1029/2010JC006312>
- Ott, M. W. (2002). An improvement in the calculation of ADCP velocities. *Journal of Atmospheric and Oceanic Technology*, *19*(10), 1738–1741. [https://doi.org/10.1175/1520-0426\(2002\)019<1738:aitco>2.0.co;2](https://doi.org/10.1175/1520-0426(2002)019<1738:aitco>2.0.co;2)
- Poff, N. L., Olden, J. D., Merritt, D. M., & Pepin, D. M. (2007). Homogenization of regional river dynamics by dams and global biodiversity implications. *Proceedings of the National Academy of Sciences*, *104*(14), 5732–5737. <https://doi.org/10.1073/pnas.0609812104>
- Pope, S. B. (2000). *Turbulent flows*. Cambridge University Press. <https://doi.org/10.1017/CBO9780511840531>
- Raymond, P. A., Hartmann, J., Lauerwald, R., Sobek, S., McDonald, C., Hoover, M., et al. (2013). Global carbon dioxide emissions from inland waters. *Nature*, *503*(7476), 355–359. <https://doi.org/10.1038/nature12760>
- Raymond, P. A., Zappa, C. J., Butman, D., Bott, T. L., Potter, J., Mulholland, P., et al. (2012). Scaling the gas transfer velocity and hydraulic geometry in streams and small rivers. *Limnology and Oceanography: Fluids and Environments*, *2*(1), 41–53. <https://doi.org/10.1215/21573689-1597669>
- Richey, J. E., Melack, J. M., Aufdenkampe, A. K., Ballester, V. M., & Hess, L. L. (2002). Outgassing from Amazonian rivers and wetlands as a large tropical source of atmospheric CO₂. *Nature*, *416*(6881), 617–620. <https://doi.org/10.1038/416617a>
- Sabrekov, A. F., Runkle, B. R. K., Glagolev, M. V., Terentieva, I. E., Stepanenko, V. M., Kotsyurbenko, O. R., et al. (2017). Variability in methane emissions from west Siberia's shallow boreal lakes on a regional scale and its environmental controls. *Biogeosciences*, *14*(15), 3715–3742. <https://doi.org/10.5194/bg-14-3715-2017>
- Scully, M. E., Geyer, W. R., & Trowbridge, J. H. (2011). The influence of stratification and nonlocal turbulent production on estuarine turbulence: An assessment of turbulence closure with field observations. *Journal of Physical Oceanography*, *41*(1), 166–185. <https://doi.org/10.1175/2010JPO4470.1>
- Stacey, M. T., Monismith, S. G., & Burau, J. R. (1999). Measurements of Reynolds stress profiles in unstratified tidal flow. *Journal of Geophysical Research: Oceans*, *104*(C5), 10933–10949. <https://doi.org/10.1029/1998JC900095>
- Stepanenko, V., Mammarella, I., Ojala, A., Miettinen, H., Lykosov, V., & Vesala, T. (2016). LAKE 2.0: A model for temperature, methane, carbon dioxide and oxygen dynamics in lakes. *Geoscientific Model Development*, *9*(5), 1977–2006. <https://doi.org/10.5194/gmd-9-1977-2016>
- Sukhodolov, A., Thiele, M., & Bungartz, H. (1998). Turbulence structure in a river reach with sand bed. *Water Resources Research*, *34*(5), 1317–1334. <https://doi.org/10.1029/98WR00269>
- Talke, S. A., Horner-Devine, A. R., Chickadel, C. C., & Jessup, A. T. (2013). Turbulent kinetic energy and coherent structures in a tidal river. *Journal of Geophysical Research: Oceans*, *118*(12), 6965–6981. <https://doi.org/10.1002/2012JC008103>
- Tedford, E. W., MacIntyre, S., Miller, S. D., & Czirkowsky, M. J. (2014). Similarity scaling of turbulence in a temperate lake during fall cooling. *Journal of Geophysical Research: Oceans*, *119*(8), 4689–4713. <https://doi.org/10.1002/2014JC010135>
- Tennekes, H., & Lumley, J. L. (1972). *A first course in turbulence*. MIT press.
- Terray, E., Donelan, M., Agrawal, Y., Drennan, W. M., Kahma, K., Williams, A. J., et al. (1996). Estimates of kinetic energy dissipation under breaking waves. *Journal of Physical Oceanography*, *26*(5), 792–807. [https://doi.org/10.1175/1520-0485\(1996\)026<0792:eokedu>2.0.co;2](https://doi.org/10.1175/1520-0485(1996)026<0792:eokedu>2.0.co;2)
- Thomson, R. E., & Emery, W. J. (2001). *Data analysis methods in physical oceanography*. Elsevier Science. <https://doi.org/10.1016/B978-0-444-50756-3.X5000-X>
- Tranvik, L. J., Downing, J. A., Cotner, J. B., Loiselle, S. A., Striegl, R. G., Ballatore, T. J., et al. (2009). Lakes and reservoirs as regulators of carbon cycling and climate. *Limnology and Oceanography*, *54*(6part2), 2298–2314. https://doi.org/10.4319/lo.2009.54.6_part_2.2298
- Ulseth, A. J., Hall, R. O., Canadell, M. B., Madinger, H. L., Niayifar, A., & Battin, T. J. (2019). Distinct air–water gas exchange regimes in low- and high-energy streams. *Nature Geoscience*, *12*(4), 259–263. <https://doi.org/10.1038/s41561-019-0324-8>
- Wahl, T. L. (2003). Discussion of “Despiking Acoustic Doppler Velocimeter Data” by Derek G. Goring and Vladimir I. Nikora. *Journal of Hydraulic Engineering*, *129*(6), 484–487. [https://doi.org/10.1061/\(asce\)0733-9429\(2003\)129:6\(484\)](https://doi.org/10.1061/(asce)0733-9429(2003)129:6(484))
- Wallin, M. B., Campeau, A., Audet, J., Bastviken, D., Bishop, K., Kocik, J., et al. (2018). othersCarbon dioxide and methane emissions of Swedish low-order streams—A national estimate and lessons learnt from more than a decade of observations. *Limnology and Oceanography Letters*, *3*(3), 156–167. <https://doi.org/10.1002/lo2.10061>

- Wang, B., Liao, Q., Fillingham, J. H., & Bootsma, H. A. (2015). On the coefficients of small eddy and surface divergence models for the air-water gas transfer velocity. *Journal of Geophysical Research: Oceans*, *120*(3), 2129–2146. <https://doi.org/10.1002/2014JC010253>
- Wang, B., Liao, Q., Xiao, J., & Bootsma, H. A. (2013). A free-floating PIV system: Measurements of small-scale turbulence under the wind wave surface. *Journal of Atmospheric and Oceanic Technology*, *30*(7), 1494–1510. <https://doi.org/10.1175/JTECH-D-12-00092.1>
- Wüest, A., & Lorke, A. (2003). Small-scale hydrodynamics in lakes. *Annual Review of Fluid Mechanics*, *35*(1), 373–412. <https://doi.org/10.1146/annurev.fluid.35.101101.161220>
- Zappa, C. J., McGillis, W. R., Raymond, P. A., Edson, J. B., Hints, E. J., Zemmelen, H. J., et al. (2007). Environmental turbulent mixing controls on air-water gas exchange in marine and aquatic systems. *Geophysical Research Letters*, *34*(10). <https://doi.org/10.1029/2006GL028790>